Research paper

Comparison study on mooring line models for hydrodynamic performances of floating offshore wind turbines

Wenjie Zhong [a], Weiwen Zhao [a], Decheng Wan [a,*], Yan Zhao [b]

[a] Computational Marine Hydrodynamics Lab (CMHL), School of Naval Architecture, Ocean and Civil Engineering, Shanghai Jiao Tong University, Shanghai, China
[b] Key Laboratory of Far-shore Wind Power Technology of Zhejiang Province, Huadong Engineering Corporation Limited, Hangzhou, China

ARTICLE INFO

ABSTRACT

The mooring system plays a crucial role in the seakeeping ability of floating offshore wind turbines (FOWTs) but complicates the overall dynamics of the system. Many quasi-static (QS) and dynamic models for mooring analysis exist but a comprehensive comparison among open-source or semi open-source codes in various scenarios is rare. In the present study, six mooring models including three dynamic and three QS ones are assessed. The three dynamic models are the local discontinuous Galerkin (LDG) finite element method (FEM), the lumped mass (LM) method and the finite different method (FDM), and the three QS models are the piecewise extrapolation method (PEM), the catenary and the QS of MAP. Three groups of tests involving catenary line under fairlead excitation, hanging line with axial excitation and FOWT in waves are conducted. The first two test groups focus on single line dynamics to assess among the three dynamic models while the third test group focuses on coupled hydro-mooring modeling with the FEM, PEM, catenary and QS coupled to OpenFOAM. The test results show that there are substantial differences among the models in various scenarios. And the LDG FEM and LM models are recommended to be applied in realistic FOWT hydrodynamics problems.

1. Introduction

The interests in deploying the floating offshore wind turbines (FOWTs) for extracting wind energy in deep waters urge comprehensive research on their dynamic properties in various sea states and operational conditions. FOWT is featured as a multi-body system comprising the rotor and nacelle, the tower, the platform and the mooring system, and the coupling among the components makes its dynamics a challenge to simulate (Antonutti et al., 2016; Liu et al., 2017; Tran and Kim, 2016). For interests of the present study, the reaction from moorings complicates the dynamics of the structure while serving to provide its sea-keeping ability. The dynamics of the mooring system affects the line tensions, the fatigue and extreme loads of other components, the global damping of the floating platform, and the motion responses of the complete structure (Hall et al., 2014; Kallesøe and Hansen, 2011; Masciola et al., 2013b). The mooring system is thus of great significance for the power generation of the mounted wind turbines (Ren et al., 2022).

For modeling moorings in a FOWT design, both quasi-static (QS) and dynamic approaches are feasible candidates. The QS solves for the mooring position and tension assuming that the line is in static equilibrium, and is popular in use for FOWTs as it is computationally efficient, easy to work with, and available in open-source codes, e.g., Masciola et al. (2013a). Numerous computational fluid dynamics (CFD) researchers used QS models for coupled hydro-mooring (Huang et al., 2021; Tran and Kim, 2015) or coupled aero-hydro-mooring (Cheng et al., 2019; Liu et al., 2017, 2019; Tran and Kim, 2016) analysis of FOWTs. The weakness of QS is that the hydrodynamic and inertial forces are ignored. These dynamic effects are included in dynamic mooring models which are widely used in analytical codes of FOWTs, e.g., Dai et al. (2018), Jonkman (2009) and Robertson et al. (2014b). One well-known code is the OpenFAST which is capable of conducting fully coupled time-domain aero-hydro-servo-elastic analysis of FOWTs. There have been several studies conducted to compare the QS and dynamic mooring line models in coupled FOWT analysis. The conclusions indicate that the inclusion of mooring dynamics is in many cases necessary for accurately predicting the mooring loads and FOWT dynamics. For example, Kallesøe and Hansen (2011) compared the coupled analysis results of a spar-buoy FOWT with dynamic FEM and QS lookup-table mooring models. They observed that the FEM model predicts similar blade loads but lower tower loads comparing to the QS in normal

* Corresponding author.
  E-mail address: dcwan@sjtu.edu.cn (D. Wan).

conditions. Matha et al. (2011) carried out a comparison study using the Hywind design and a multi-body mooring line model, and found that the dynamic model gives smaller platform motions but larger mooring fatigue loads than QS. Masciola et al. (2013b) analyzed the response of the DeepCwind in coupled simulations by FAST with the mooring line modeled by OrcaFlex and MAP, respectively. They found that the mooring dynamics modifies the platform motions only in extreme sea states but the mooring line tensions are affected in all load cases. Similar conclusions were drawn in Hall et al. (2014), where the FEM and QS mooring line models were used for three classes of FOWT designs. The implications of the findings for selecting mooring models are that the aero-hydro-elastic analysis of FOWTs incorporating mooring dynamics is necessary for evaluating mooring line loads in both mild and severe environmental conditions. It is pointed out that the comparison studies in above literature used analytical FOWT codes while comparisons in the framework of CFD are rare.

There are mainly four types of dynamic mooring models, i.e., lumped mass (LM) method, FEM, finite difference method (FDM), and multi-body dynamics (MBD) method. The LM was introduced for mooring modeling at the end of 1950's despite that the model was simple and neglected the material elasticity and the line-seabed contact (Walton and Polachek, 1959). The line elasticity and seabed reaction were incorporated into mooring modeling in Wilhelmy et al. (1981) and Nakajima et al. (1982), and the improved model was validated via forced harmonic oscillation tests. Khan and Ansari (1986) proposed a 3D LM model, in which the masses are concentrated at nodes of rigid line segments. The model was demonstrated with capabilities of line-seabed contact and clump weights. Recently, Hall and Goupee (2015) developed an open-source LM code to be used for standalone and coupled simulations, and validated the model against tension measurements of the DeepCwind mooring lines obtained by scaled tests in wave tank. The code has been officially included into the OpenFAST package for coupled aero-hydro-servo-elastic analysis of FOWTs. The LM code has also been implemented into the open-source CFD library OpenFOAM for coupled analysis of moored floating structures (Jiang et al., 2020). Other LM variants have been implemented and applied in marine engineering mooring analysis (Touzon et al., 2020; Hermawan and Furukawa, 2020). The LM was extended to investigate the effects of the strain and strain rate dependent stiffness on the dynamics of FOWTs with catenary and taut mooring systems in Li and Choung (2021). Numerous FEM models are available, for instance, the typical model ignoring the bending stiffness (Aamo and Fossen, 2000) and the comprehensive model including bending and torsion effects (Buckham et al., 2004). Formulations based on high-order finite elements (Escalante et al., 2011) and mixed finite elements (Montano et al., 2007) have also been presented. More recently, Palm et al. (2017) developed a FEM model using the local discontinuous Galerkin (LDG) FEM with the aim of better modeling snap loads than traditional numerical approaches. The model was validated against laboratory experiments. In Zhang et al. (2022a), a dynamic model of catenary mooring line was developed based on the vector form intrinsic finite element (VFIFE) method, and was verified via experimental data and other validated models. The VFIFE method has been used for the dynamic analysis of marine risers by Li et al. (2018), and the static and dynamic analyses of marine pipes by Wu et al. (2020). The results showed the feasibility of VFIFE in the nonlinear motion analysis of marine structures. The VFIFE method was also used in building a modeling framework of FOWTs (Zhang et al., 2022b). In the framework, the MBD is used to handle the rigid body motion, and the analysis of structural deformation and the solution of motion equations are conducted based on VFIFE. The FDM and MBD mooring models are relatively less applied in literature. A 3D FDM that incorporates the line elasticity was developed by Huang (1994), and was demonstrated via modeling a subsea unit towed by a maneuvering vessel. Recently, a FDM mooring dynamics model was developed by Chen et al. (2018) and has been used for the model-based analysis of FOWTs. It is found on review that comparisons of dynamic mooring line models are rare in literature.

In this study, performances of six mooring line models including three dynamic and three QS ones, are compared. The three dynamic models are the LDG FEM of Moody (Palm et al., 2017), the LM of MoorDyn (Hall and Goupee, 2015) and the FDM of OpenMOOR (Chen et al., 2018). And the three QS models are the piecewise extrapolation method (PEM), the catenary and the QS of MAP (Masciola et al., 2013a). The Moody, MoorDyn, OpenMOOR and MAP are open-source or semi open-source codes while the PEM and catenary mooring models are developed by the research group of the authors. Three categories of tests including catenary cable subjected to fairlead excitation, hanging cable with axial excitation and semi-submersible FOWT in waves are carried out. The first two test categories focus on single line dynamics to analyze among the three dynamic models. In the third test category, four hydro-mooring models are built with the FEM, PEM, catenary and QS coupled to OpenFOAM, and performances of the quasi-static and dynamic mooring models are compared for FOWT hydrodynamics in the CFD framework. The aim of the present study is to obtain deep insights into performances of various mooring line models, and attempts to give suggestions for choices of mooring models in FOWT analysis.

The remainder of the paper is organized as follows. Details of the six mooring line models are given in the next section. The three categories of tests, i.e., dynamics of catenary cable due to fairlead excitation, dynamics of hanging cable under axial excitation and hydrodynamics of a 15 MW semi-submersible FOWT under wave impacts, are described in sections 3, 4 and 5, respectively. In each of the three sections, the physical problem, the numerical details and the results are presented in sequence. Finally, the conclusions are made in section 6.

2. Mooring line models

2.1. LDG FEM

The mooring dynamics represented with LDG FEM from Palm et al. (2017) is used. The dynamics of flexible mooring lines is governed by a vector-valued wave equation expressed in the global inertia frame as

$$\frac{\partial^2 \boldsymbol{r}}{\partial t^2} = \frac{1}{\gamma_0} \frac{\partial \boldsymbol{T}}{\partial s} + \frac{\boldsymbol{f}}{\gamma_0} \tag{1}$$

where γ_0 is the mooring line mass per meter. $\boldsymbol{R}$ denotes the cable position in the reference frame and s is the curvilinear abscissa along the unstretched line.

For numerical reasons, a first order equation system in terms of a state vector $\boldsymbol{u}$ comprising the cable position $\boldsymbol{r}$, its spatial derivative $\boldsymbol{q}$ and the momentum density ν can be made as

$$\dot{\boldsymbol{u}} = \frac{\partial F(\boldsymbol{u})}{\partial s} + Q(\boldsymbol{u}) \tag{2}$$

where

$$\boldsymbol{u} = [\boldsymbol{r}, \boldsymbol{q}, \nu] \tag{3}$$

$$\boldsymbol{F}(\boldsymbol{u}) = \left[\varnothing, \frac{\nu}{\gamma_0}, \boldsymbol{T} \right]^T \tag{4}$$

$$\boldsymbol{Q}(\boldsymbol{u}) = \left[\frac{\nu}{\gamma_0}, \varnothing, \boldsymbol{f} \right]^T \tag{5}$$

In the mooring dynamics, only the extensional stiffness is included while the bending and torsional stiffnesses are ignored. The internal moment $\boldsymbol{M}$ is set to zero in the modeling, and the axial tension force vector $\boldsymbol{T}$ is tangential to the cable as

$$\boldsymbol{T} = T(\varepsilon, \dot{\varepsilon}) \frac{\boldsymbol{q}}{1 + \varepsilon} \tag{6}$$

$$\varepsilon = |\boldsymbol{q}| - 1 \tag{7}$$

where ε is the axial strain. T is the magnitude of tension which contains the constitutive relation of the mooring line as a function of strain and strain rate. For a linear elastic cable, the tension expresses as $T = EA\varepsilon$. For completeness, the strain rate is numerically calculated as

$$\dot{\varepsilon}^{(k)} = \frac{\dot{\boldsymbol{q}}^{(k-1)} \cdot \boldsymbol{q}^{(k)}}{1 + \varepsilon^{(k)}} \tag{8}$$

where the superscripts $(k-1)$ and (k) indicate at which time step the variables are evaluated.

The symbol $\boldsymbol{f}$ represents all external forces on the mooring line as

$$\boldsymbol{f} = \boldsymbol{f}_a + \boldsymbol{f}_b + \boldsymbol{f}_c + \boldsymbol{f}_d \tag{9}$$

$\boldsymbol{f}_a$ includes the inertia force and the added mass force which exist for structures accelerating in fluids as

$$\boldsymbol{f}_a = \rho_f A_0 \left(C_{at} \boldsymbol{a}_{r,t} + C_{an} \boldsymbol{a}_{r,n} + \boldsymbol{a}_f \right) \tag{10}$$

where C_a is the added mass coefficient, and subscripts t and n mean the tangential and normal directions respectively. $\boldsymbol{A}$ is the acceleration vector. A_0 is the cross-sectional area of unstretched cable line.

$\boldsymbol{F}_b$ is the net force from buoyancy written as

$$\boldsymbol{f}_b = \gamma_0 \frac{\rho_c - \rho_f}{\rho_c} \boldsymbol{g} \tag{11}$$

where ρ_c and ρ_f are the density of the mooring line and fluid, respectively.

$\boldsymbol{F}_c$ is the contact force between the mooring line and the seabed. The bilinear spring-damper model is used for the normal force to the contact plane and dynamic friction is implemented for the tangential force. For a horizontal sea floor, the contact force vector is given as

$$\boldsymbol{f}_c = \begin{cases} \boldsymbol{G}_v + \boldsymbol{G}_h & \text{if} (z_G - r_z) \geq 0 \\ 0 & \text{otherwise} \end{cases} \tag{12}$$

$$\boldsymbol{G}_v = \left(K_G d_c (z_G - r_z) - 2\xi_G \sqrt{K_G \gamma_0 d_c} \max(\dot{r}_z, 0) \right) \boldsymbol{z} \tag{13}$$

$$\boldsymbol{G}_h = \mu f_{b_z} \tanh \left(\frac{\pi \dot{r}_{xy}}{v_\mu} \right) \frac{\dot{\boldsymbol{r}}_{xy}}{|\dot{\boldsymbol{r}}_{xy}|} \tag{14}$$

where z_G is the vertical position of the seabed. K_G and ξ_G are the stiffness and ratio of critical damping for the cable-seabed interaction, respectively. μ is the friction coefficient with a user-specified velocity v_μ for maximum friction.

$\boldsymbol{F}_d$ is the drag proportional to the square of the relative velocity between the structure and fluid as

$$\boldsymbol{f}_d = \rho_f d \sqrt{1 + \varepsilon} \left(C_{Dt} |v_{r,t}| \boldsymbol{v}_{r,t} + C_{Dn} |v_{r,n}| \boldsymbol{v}_{r,t} \right) \Big/ 2 \tag{15}$$

where C_D is the drag coefficient, and $\boldsymbol{v}$ is the velocity vector. Note that the drag is modeled for circular cross-sections with volume-preserving property during axial strain, and the elongation and contraction factors do not fully cancel which leads to a multiplier in the definition.

The LDG FEM with Legendre basis functions φ_k of arbitrary order p is used to spatially discretize the dynamic equation. The discontinuity between elements emerges when deriving the weak form of the governing equation with the numerical flux represented by terms with straight overbar in Eq. (16). The equation is manipulated on the eth element with the boundaries denoted by s_l^e and s_u^e as shown in Fig. 1.

$$\int_{\Omega^e} \varphi_k \varphi_i ds \frac{\partial \tilde{\boldsymbol{u}}^e}{\partial t} = \int_{\Omega^e} \varphi_k \frac{\partial \varphi_i}{\partial s} ds \tilde{\boldsymbol{F}}^e + \left[\varphi_k (\overline{\boldsymbol{F}^e} - \boldsymbol{F}^e) \right] \Big|_{s_l^e}^{s_u^e} + \int_{\Omega^e} \varphi_k \boldsymbol{Q}^e ds \tag{16}$$

$\forall k, i \in [0, p]$. The elemental integrals are evaluated by the Gauss-Lobatto-Legendre quadrature points and quadrature rules. The key step of LDG is that the boundary integral is approximated by a numerical
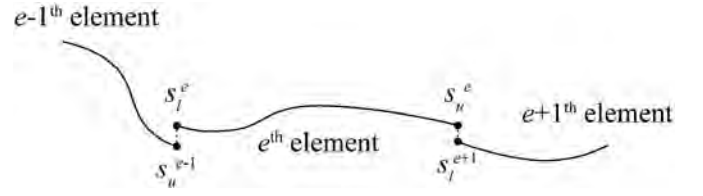

Fig. 1. Discontinuity across segments in the LDG FEM mooring line model.

flux. As the elements are discontinuous at boundaries, the numerical flux enables the coupling between elements. The numerical flux is evaluated via the local Lax-Friedrich flux (Bernard, 2008) as:

$$\overline{\boldsymbol{F}^e} = \{\boldsymbol{F}^e\} + |\lambda|_{\max} [\boldsymbol{u}^e] \tag{17}$$

where

$$\{\boldsymbol{F}^e\} = 0.5(\boldsymbol{F}^+ + \boldsymbol{F}^-) \tag{18}$$

$$[\boldsymbol{u}^e] = 0.5(\boldsymbol{n}^+ \boldsymbol{u}^- + \boldsymbol{n}^- \boldsymbol{u}^+) \tag{19}$$

where superscripts $+$ and $-$ on $\boldsymbol{F}$ and $\boldsymbol{u}$ mean taking values from the internal and external sides of the elemental boundary, respectively. The normal vector $\boldsymbol{n}$ points outward such that for each line element, $\boldsymbol{n}^+ = -1$ on s_l^e and $\boldsymbol{n}^+ = +1$ on s_u^e.

The maximum eigenvalue in Eq. (17) is chosen as

$$|\lambda|_{\max} = \begin{cases} 0.8 \left| \frac{[\boldsymbol{F}^e]}{[\boldsymbol{u}^e]} \right| & \text{if } u = q \\ |c_t| & \text{otherwise} \end{cases} \tag{20}$$

where c_t is the tangential wave speed in the cable, and is defined by the maximum eigenvalue of the hyperbolic problem as

$$c_t = \sqrt{\frac{\partial T}{\partial \varepsilon} \gamma_0} \tag{21}$$

The mooring domain boundaries are of Dirichlet or Neumann types. Dirichlet conditions control the position and the momentum while Neumann conditions provide the tension. Thus, the fluxes on domain boundaries are obtained as

$$\boldsymbol{F}^- = [\varnothing, \nu_D, \boldsymbol{T}^+]^T \text{ and } \boldsymbol{u}^- = [\boldsymbol{r}_D, \boldsymbol{q}^+, \nu_D \gamma_0]^T \text{ on } \Gamma_D \tag{22}$$

$$\boldsymbol{F}^- = \left[\varnothing, \frac{\nu^+}{\gamma_0}, \boldsymbol{T}_N \right]^T \text{ and } \boldsymbol{u}^- = [\boldsymbol{r}^+, |\boldsymbol{q}^+| \boldsymbol{t}_N, \nu^+]^T \text{ on } \Gamma_N \tag{23}$$

where superscript $+$ again means using value from internal side of the boundary. Note that the tension condition is weakly embodied in the q equation as the correct direction of the force is enforced while retaining the norm of the internal field. The tension magnitude is prescribed through the force flux in the momentum equation.

Eq. (16) advances in time with the strong-stability-preserving third-order explicit Runge-Kutta scheme (Cockburn and Shu, 2001). A hp-adaptive mesh refinement scheme is used for limiting the numerical error below a preset tolerance ε^*. In the mooring line model, the tension magnitude T is selected as the indicator variable for the solution quality. For smooth solutions, a convergence rate of $O(h^{p+1})$ is expected, but in the presence of discontinuities, the solution converges as $O(h)$ (Krivodonova et al., 2004). The relative jump defined in Barter and Darmofal (2010) is used in Bernard's formula for the numerical error (Bernard, 2008) as

$$\varepsilon^e = \frac{1}{\sqrt{8}} \sqrt{\left(\left| \frac{[T]}{\{T\}} \right|_{s_l^e} \right)^2 + \left(\left| \frac{[T]}{\{T\}} \right|_{s_u^e} \right)^2} \tag{24}$$

In order to locate the regions of sharp gradients or shocks, the nature of the numerical error is assessed through the shock indicator defined as

$$I^e = \max \left(\left. \left| \frac{[T]}{\{T\}} \right| \right|_{s_l^e}, \left. \left| \frac{[T]}{\{T\}} \right| \right|_{s_u^e} \right) h^{-0.5(p+1)} \tag{25}$$

which rapidly grows to infinity near discontinuities and is small in smooth regions. Considering the case of cable slack condition where a snap load is expected to emerge in the near future, the shock criteria are collectively formulated as

$$S^e = \begin{cases} 1 & \text{if } I^e \geq 1 \text{ and } \varepsilon^e \geq \varepsilon^* \\ 1 & \text{if } \min(T^e) \leq T^* \\ 0 & \text{otherwise} \end{cases} \tag{26}$$

For the hp-adaptivity scheme, p-refinement has precedence over h-refinement in elements of smooth solutions with errors larger than the tolerance. If shocks occur, the element is raised to maximum h-refinement and the order reduces to linear ($p = 1$). The h-refinement is restricted to splitting elements in half and merging two equally sized elements with the same parent. The initial mesh h-resolution is not allowed to coarsen, and the splitting hierarchy of elements is thus confined to one element of the initial mesh. The control algorithm for the hp-adaptive mesh refinement is

$$\text{if } S^e = 1: p = 1, h = h_{\min}$$

$$\text{if } S^e = 0: \begin{cases} p = \min(p+1, p_{\max}) & \text{if } \varepsilon^e \geq \varepsilon^* \\ h = \max(0.5h, h_{\min}) & \text{if } \varepsilon^e \geq \varepsilon^* \text{ and } p = p_{\max} \\ h = \min(2h, h_{\max}) & \text{if } \varepsilon^e < 0.5^{p+1}\varepsilon^* \\ p = \max(p-1, 1) & \text{if } \varepsilon^e < h\varepsilon^* \text{ and } h = h_{\max} \end{cases} \tag{27}$$

In h-refinement, the Gauss-Lobatto-Legendre (GLL) quadrature points, $\xi \in [-1, 1]$, of the parent element always has the same relation to the points of its two child elements. This allows for a precomputed split map matrix between modal values of the parent and child elements as

$$\begin{bmatrix} \widetilde{\boldsymbol{u}}^- \\ \widetilde{\boldsymbol{u}}^+ \end{bmatrix} = \begin{bmatrix} \boldsymbol{M}^{-1}\boldsymbol{\varphi}^T(\xi)\boldsymbol{\varphi}(\xi_s)\varnothing \\ \varnothing \boldsymbol{M}^{-1}\boldsymbol{\varphi}^T(\xi)\boldsymbol{\varphi}(\xi_s) \end{bmatrix} \widetilde{\boldsymbol{u}} \tag{28}$$

$$\xi_s = \begin{bmatrix} 0.5(\xi-1) \\ 0.5(\xi+1) \end{bmatrix} \tag{29}$$

where superscript - and + describe values in the left and right child elements, respectively. $\boldsymbol{M}^{-1}$ is the inverse mass matrix and ξ_s denotes the projections of the GLL points of the split elements onto the parent elemental domain.

A separate transform is defined for the merging operation as in Eq. (30). Note that to avoid ambiguous midpoint of the adjacent elements, the merge map matrix is based on even number of quadrature points in the final element.

$$\widetilde{\boldsymbol{u}} = \begin{bmatrix} \boldsymbol{M}^{-1}\boldsymbol{\varphi}^T(\xi)\varnothing \\ \varnothing \boldsymbol{M}^{-1}\boldsymbol{\varphi}^T(\xi) \end{bmatrix} \begin{bmatrix} \boldsymbol{\varphi}(2\xi+1), \forall \xi < 0 \\ \boldsymbol{\varphi}(2\xi-1), \forall \xi > 0 \end{bmatrix} \begin{bmatrix} \widetilde{\boldsymbol{u}}^- \\ \widetilde{\boldsymbol{u}}^+ \end{bmatrix} \tag{30}$$

To treat unwanted overshoots near shocks, the generalized minMod slope limiter described in Cockburn and Shu (2001) is used.

$$\widetilde{\boldsymbol{u}}_1^e = \min Mod \left(\theta_l \frac{\widetilde{\boldsymbol{u}}_0^e - \widetilde{\boldsymbol{u}}_0^{e-1}}{2}, \theta_l \frac{\widetilde{\boldsymbol{u}}_0^{e+1} - \widetilde{\boldsymbol{u}}_0^e}{2}, \widetilde{\boldsymbol{u}}_1^e \right), \theta_l \in [1, 2] \tag{31}$$

where variables with subscripts 0 and 1 refer to the mean and linear slope values, respectively. The θ_l blends the limiter between the classical minMod for $\theta_l = 1$ and the less restrictive, generalized minMod for $\theta_l = 2$. The minMod function is defined as

$$\min Mod(a, b, c) = \begin{cases} \min(a, b, c) & \text{if } a, b, c > 0 \\ \max(a, b, c) & \text{if } a, b, c < 0 \\ 0 & \text{otherwise} \end{cases} \tag{32}$$

2.2.

The LM formulation of mooring dynamics from Hall and Goupee (2015) is adopted. In the LM approach, the mooring line is discretized along the length of the line, resulting in a finite number of evenly-sized segments joining $n + 1$ nodes. Fig. 2 shows that the numbering scheme for the segments and nodes of each mooring line obeys a bottom-up principle. Specifically, the node indexes for the anchor and fairlead are 0 and n, respectively. The segment between nodes 0 and 1 is given an index of $1/2$ and the last segment between nodes n - 1 and n is marked n - $1/2$. Each line is assigned identical properties, including the density (ρ_m), the unstretched length (l_m), the volume-equivalent diameter (d_m), the Young's modulus (E_m) and the internal damping coefficient (C_{int}). The mooring line segments are treated as massless while the mass is evenly distributed to the nodes joining the segment. The equation of motion for node i is given as

$$(\boldsymbol{m}_i + \boldsymbol{A}_i)\ddot{\boldsymbol{r}} = \boldsymbol{T}_{i+1/2} - \boldsymbol{T}_{i-1/2} + \boldsymbol{C}_{i+1/2} - \boldsymbol{C}_{i-1/2} + \boldsymbol{W}_i + \boldsymbol{B}_i + \boldsymbol{D}_i \tag{33}$$

where $\boldsymbol{r}_i$ ($= \{x_i, y_i, z_i\}$) and $\boldsymbol{m}_i$ ($= \rho_m \pi d_m^2 l_m \boldsymbol{I}/4$) denote the position and mass matrix of the node, respectively. The forces in Eq. (33) include the buoyancy (subtracting weight) $\boldsymbol{W}_i$, the seabed reaction force $\boldsymbol{B}_i$, the axial tension $\boldsymbol{T}_i$, the axial damping $\boldsymbol{C}_i$, the hydrodynamic added mass $\boldsymbol{A}_i$ and drag $\boldsymbol{D}_i$ (see Fig. 2). Expressions for the forces are given as follows.

$$\boldsymbol{W}_i = \frac{1}{2} \left(\boldsymbol{W}_{i+1/2} + \boldsymbol{W}_{i-1/2} \right) = (\rho_m - \rho_w)\pi d_m^2 l_m \boldsymbol{g} \Big/ 4 \tag{34}$$

$$\boldsymbol{B}_i = d_m l_m [(z_{bot} - z_i)k_b - \dot{z}_i c_b]\boldsymbol{e}_z \tag{35}$$

$$\boldsymbol{T}_{i+1/2} = E_m \pi d_m^2 \left(\frac{1}{l_m} - \frac{1}{|\boldsymbol{r}_{i+1} - \boldsymbol{r}_i|} \right)(\boldsymbol{r}_{i+1} - \boldsymbol{r}_i) \Big/ 4 \tag{36}$$

$$\boldsymbol{T}_{i-1/2} = -E_m \pi d_m^2 \left(\frac{1}{l_m} - \frac{1}{|\boldsymbol{r}_i - \boldsymbol{r}_{i-1}|} \right)(\boldsymbol{r}_i - \boldsymbol{r}_{i-1}) \Big/ 4 \tag{37}$$

$$\boldsymbol{C}_{i+1/2} = C_{int}\pi d_m^2 \frac{1}{l_m} \frac{(\boldsymbol{r}_{i+1} - \boldsymbol{r}_i)}{|\boldsymbol{r}_{i+1} - \boldsymbol{r}_i|^2} [(x_{i+1} - x_i)(\dot{x}_{i+1} - \dot{x}_i) + (y_{i+1} - y_i)(\dot{y}_{i+1}$$
$$- \dot{y}_i) + (z_{i+1} - z_i)(\dot{z}_{i+1} - \dot{z}_i)] \Big/ 4 \tag{38}$$

$$\boldsymbol{C}_{i-1/2} = -C_{int}\pi d_m^2 \frac{1}{l_m} \frac{(\boldsymbol{r}_i - \boldsymbol{r}_{i-1})}{|\boldsymbol{r}_i - \boldsymbol{r}_{i-1}|^2} [(x_i - x_{i-1})(\dot{x}_i - \dot{x}_{i-1}) + (y_i - y_{i-1})(\dot{y}_i$$
$$- \dot{y}_{i-1}) + (z_i - z_{i-1})(\dot{z}_i - \dot{z}_{i-1})] \Big/ 4 \tag{39}$$

$$\boldsymbol{A}_i\ddot{\boldsymbol{r}}_i = \boldsymbol{A}_{qi}\ddot{\boldsymbol{r}}_i + \boldsymbol{A}_{pi}\ddot{\boldsymbol{r}}_i = \rho_w \pi d_m^2 l_m \left[C_{at}\boldsymbol{a}_{qi} + C_{an}\boldsymbol{a}_{pi} \right] \Big/ 4 \tag{40}$$

$$\boldsymbol{D}_i = \boldsymbol{D}_{qi} + \boldsymbol{D}_{pi} = \rho_w d_m l_m \left\{ \pi C_{dt}\boldsymbol{U}_{qi} |\boldsymbol{U}_{qi}| + C_{dn}\boldsymbol{U}_{pi} |\boldsymbol{U}_{pi}| \right\} \Big/ 2 \tag{41}$$

The hydrodynamic forces on line segments are calculated with Morison equation, and C_{at}, C_{an}, C_{dt} and C_{dn} denote the tangential and transverse added mass coefficients, tangential and transverse drag coefficients respectively. Quiescent water is assumed in hydrodynamic analysis. Thus, the relative water velocity over node i is taken as ($-\dot{\boldsymbol{r}}_i$). To resolve the relative velocities and accelerations into transverse and tangential components, the tangent direction $\boldsymbol{q}_i$ at node i is defined as the average of the tangent directions of two adjacent segments (see Fig. 2), and is calculated by $\boldsymbol{q}_i = (\boldsymbol{r}_{i+1} - \boldsymbol{r}_{i-1})/|\boldsymbol{r}_{i+1} - \boldsymbol{r}_{i-1}|$. Thus, the tangential component of the relative velocity is given by $\boldsymbol{U}_{qi} = (-\dot{\boldsymbol{r}}_i \cdot \boldsymbol{q}_i)\boldsymbol{q}_i$. The transverse direction $\boldsymbol{p}_i$ is perpendicular to $\boldsymbol{q}_i$ and on an identical plane with ($-\dot{\boldsymbol{r}}_i$), and the transverse component of the velocity is given as $\boldsymbol{U}_{pi} = (\dot{\boldsymbol{r}}_i \cdot \boldsymbol{q}_i)\boldsymbol{q}_i - \dot{\boldsymbol{r}}_i$. In a similar way, the tangential and transverse components of the acceleration are $\boldsymbol{a}_{qi} = (-\ddot{\boldsymbol{r}}_i \cdot \boldsymbol{q}_i)\boldsymbol{q}_i$ and $\boldsymbol{a}_{pi} = (\ddot{\boldsymbol{r}}_i \cdot \boldsymbol{q}_i)\boldsymbol{q}_i - \ddot{\boldsymbol{r}}_i$, respectively. The seabed vertical reaction force when a node contacts the seabed is

Fig. 2. Schematic of the LM mooring line model.

considered with a linear spring-damper approach. K_b and c_b in **Eq. (35)** represent the stiffness and viscous damping per unit area of the seabed, respectively. **Eq. (35)** is only active when a node touches the seabed, i. e., $z_i < z_{bot}$. Horizontal friction from contact with the seabed is not implemented.

The second-order system of ordinary differential equation **(33)** are reduced to a system of first-order differential equations, and then solved via a constant-time-step second-order Runge–Kutta (RK2) integration algorithm.

2.3. FDM

The FDM dynamic mooring line model from Chen et al. (2018) is used. The formulation for mooring dynamics is built in Frenet frame with local x, y and z coordinates aligned with the tangential, normal and binormal directions of the curved line respectively as shown in **Fig. 3**. The Lagrangian coordinate system is parametrized by arc length s along the unstretched line and two angles φ and θ. A fixed Cartesian coordinate system (x_0, y_0, z_0) is also defined for each mooring line as seen in **Fig. 3**. The origin of the Cartesian coordinate is set at the anchor with x_0 pointing upwards and the $x_0 - y_0$ plane is the vertical plane defined by the anchor and the initial fairlead. The horizontal and vertical distances between anchor and initial fairlead are denoted as l_c and h_c, respectively.

Fig. 3. Coordinate systems of a mooring line in the FDM mooring line model.

The line position in the Cartesian coordinate system can be computed with s, φ, θ and the strain ε after solving the equations in the Lagrangian coordinate system as shown below.

$$\frac{\partial \varepsilon}{\partial s} - \frac{m}{f'(\varepsilon)}\frac{\partial u}{\partial t} + \frac{m}{f'(\varepsilon)}v\cos\theta\frac{\partial\varphi}{\partial t} - \frac{m}{f'(\varepsilon)}w\frac{\partial\theta}{\partial t} + \beta\frac{\partial\varepsilon}{\partial t} + \frac{S_b\kappa_2}{f'(\varepsilon)} - \frac{S_n\kappa_3}{f'(\varepsilon)}$$
$$- \frac{w_0}{f'(\varepsilon)}\cos\varphi\cos\theta + \frac{F_{dt}}{f'(\varepsilon)}$$
$$= 0 \tag{42}$$

$$\frac{\partial S_n}{\partial s} - (m+m_{an})\frac{\partial v}{\partial t}$$
$$- m(u\cos\theta + w\sin\theta)\frac{\partial\varphi}{\partial t} + f(\varepsilon)\kappa_3 + S_b\kappa_3\tan\theta + w_0\sin\varphi + F_{dn} = 0 \tag{43}$$

$$\frac{\partial S_b}{\partial s} - (m+m_{an})\frac{\partial w}{\partial t} + mv\sin\theta\frac{\partial\varphi}{\partial t} + mu\frac{\partial\theta}{\partial t} + C_m\rho\frac{\pi d^2}{4} - S_n\kappa_3\tan\theta - f(\varepsilon)\kappa_2$$
$$- w_0\cos\varphi\sin\theta + F_{db} = 0 \tag{44}$$

$$EI\frac{\partial\kappa_2}{\partial s} + (EI - GJ)\kappa_3{}^2\tan\theta - S_b(1+\varepsilon)^3 = 0 \tag{45}$$

$$EI\frac{\partial\kappa_3}{\partial s} + (GJ - EI)\kappa_3\kappa_2\tan\theta + S_n(1+\varepsilon)^3 = 0 \tag{46}$$

$$\frac{\partial u}{\partial s} - \frac{\partial\varepsilon}{\partial t} + \kappa_2 w - \kappa_3 v = 0 \tag{47}$$

$$\frac{\partial v}{\partial s} - (1+\varepsilon)\cos\theta\frac{\partial\varphi}{\partial t} + \kappa_3(u+w\tan\theta) = 0 \tag{48}$$

$$\frac{\partial w}{\partial s} + (1+\varepsilon)\frac{\partial\theta}{\partial t} - \kappa_3 v\tan\theta - \kappa_2 u = 0 \tag{49}$$

$$\frac{\partial\varphi}{\partial s} - \frac{\kappa_3}{\cos\theta} = 0 \tag{50}$$

$$\frac{\partial\theta}{\partial s} - \kappa_2 = 0 \tag{51}$$

where equations (42)–(44) represent force balances in the three directions of the local frame, and equations (45) and (46) are the moment balances ignoring distributed external moments. Equations (47)–(49) are the compatibility relations, and equations (50) and (51) are the

definition of material curvatures. In these equations, w_0 is the submerged mooring weight per unit length; $f(\varepsilon)$ is the axial tension; S_n and S_b are the in-plane and out-of-plane shear forces, respectively; u, v and w are the tangential, normal and binormal velocities, respectively; κ_3 and κ_2 are the in-plane and out-of-plane material curvatures, respectively; d, m, EI and GJ are the circular cross-section diameter, the mass per unit length, the bending and torsional stiffnesses, respectively; m_{an} ($=C_{an}\rho\pi d^2/4$) is the added mass in the normal direction; C_m is the inertia coefficient. A proportional structural damping is included in the formulation as (Azcona et al., 2017)

$$F_{sd} = \beta f'(\varepsilon)\frac{\partial\varepsilon}{\partial t} \tag{52}$$

where β is the damping coefficient with unit s/m.

Hydrodynamic drags in the tangential, normal, and binormal directions are computed by

$$F_{dt} = -\frac{1}{2}\rho d\pi C_{dt}u|u|\sqrt{1+\varepsilon} \tag{53}$$

$$F_{dn} = -\frac{1}{2}\rho d C_{dn}v\sqrt{v^2+w^2}\sqrt{1+\varepsilon} \tag{54}$$

$$F_{db} = -\frac{1}{2}\rho d C_{db}w\sqrt{v^2+w^2}\sqrt{1+\varepsilon} \tag{55}$$

where C_{dt}, C_{dn} and C_{db} are the drag coefficients in the three local directions.

For the seabed reaction to mooring contact, an elastic foundation is implemented while the horizontal friction is ignored. The seabed reaction force acts in the vertical direction and its role is to reduce the wet weight of the line part grounded on the seabed. The effective wet weight of the mooring line is defined as

$$w_e(s_i) = w_0 + k_s x_c(s_i) \tag{56}$$

where k_s is the seabed stiffness and s_i is the line coordinate of node i. In Chen et al. (2018), it is stated that the dynamic solution is insensitive to k_s which can be chosen such that the mooring wet weight is balanced by the seabed completely when $x_c(s_i) = -d$, i.e., $k_s = w_0/d$.

The ten equations (42)–(51) for the mooring motions can be written in a vector form as

$$M\frac{\partial Y}{\partial t} + K\frac{\partial Y}{\partial s} + F(Y, s, t) = 0 \tag{57}$$

where $Y = [\varepsilon, S_n, S_b, u, v, w, \varphi, \theta, \kappa_2, \kappa_3]$.

For numerical solution of the equation set (57), the box method and generalized-α method are adopted for the spatial and temporal discretization, respectively. In the spatial discretization, a set of $n-1$ matrix equations (n nodal points along the line and one equation per half grid point) can be derived as

$$\widetilde{M}_{j-1/2}\begin{bmatrix}\dot{Y}_{j-1}\\\dot{Y}_j\end{bmatrix} + \widetilde{K}_{j-1/2}\begin{bmatrix}Y_{j-1}\\Y_j\end{bmatrix} + \widetilde{F}_{j-1/2} = 0 \tag{58}$$

where the dot over Y signifies its differentiation with respect to time and the subscript j means the node number. The matrices and vectors have dimensions $N \times 2N$ and $N \times 1$, respectively (N is the number of dependent variables at each node, i.e., ten for the present problem). To close the equation set, N extra equations provided by the boundary conditions are needed. Zero curvature boundary conditions at the fixed anchor and fairlead of the mooring line are introduced as

$$u^{(1)} = 0, v^{(1)} = 0, w^{(1)} = 0, \kappa_2^{(1)} = 0, \kappa_3^{(1)} = 0 \tag{59}$$

$$\kappa_2^{(N)} = 0, \kappa_3^{(N)} = 0 \tag{60}$$

where the superscripts (1) and (N) denote the anchor and fairlead nodes,

respectively.

The other three boundary conditions for the dynamics of the system under induced motion of the top of the mooring line are given in terms of the fairlead velocity denoted by U_t, V_t and W_t as

$$U_t = (u\cos\varphi\cos\theta - v\sin\varphi + w\cos\varphi\sin\theta)^{(N)} \tag{61}$$

$$V_t = (u\sin\varphi\cos\theta + v\cos\varphi + w\sin\varphi\sin\theta)^{(N)} \tag{62}$$

$$W_t = (-u\sin\theta + w\cos\theta)^{(N)} \tag{63}$$

Incorporating the boundary conditions, the semi-discrete equation of motion for all of the dependent variables at all of the nodes reduces to

$$\widetilde{M}\dot{Y} + \widetilde{K}Y + \widetilde{F} = 0 \tag{64}$$

For temporal discretization, the generalized-α method given in Gobat and Grosenbaugh (2001) is used to avoid issues of Crank-Nicholson noise and lack of numerical dissipation. In the generalized-α method, temporal weighted averaging of the velocity, displacement and force vectors applied to Eq. (64) leads to a semi-discrete equation of the form

$$(1-\alpha_m)\widetilde{M}\dot{Y}^i + \alpha_m\widetilde{M}\dot{Y}^{i-1} + (1-\alpha_k)\widetilde{K}Y^i + \alpha_k\widetilde{K}Y^{i-1} + (1-\alpha_k)\widetilde{F}^i + \alpha_k\widetilde{F}^{i-1} = 0 \tag{65}$$

The temporal difference equation is the same as for the generalized trapezoidal rule.

$$Y^i = Y^{i-1} + \Delta t[(1-\gamma)\dot{Y}^{i-1} + \gamma\dot{Y}^i] \tag{66}$$

The three parameters, i.e., α_m, α_k and γ, together define the generalized-α method. And a number of algorithms can be realized through the generalized-α method. For example, the box method is implemented when the three parameters are all set to 0.5. The scheme can be reduced to a one-parameter algorithm by requiring the second-order accuracy, i. e., α_m - α_k + γ = 0.5, and enforcing eigenvalues of the amplification matrix to be real and equal as the frequency variable goes to infinity. The three parameters of the generalized-α method are then calculated by

$$\alpha_k = \frac{\lambda^\infty}{\lambda^\infty - 1}, \alpha_m = \frac{3\lambda^\infty + 1}{2\lambda^\infty - 2}, \gamma = \frac{-1}{\lambda^\infty - 1} \tag{67}$$

where λ^∞ is the value of the eigenvalue at infinity. For the parameter λ^∞, there does not appear to be a clear approach to choosing an optimal value. Gobat and Grosenbaugh (2006) found that values between -0.3 and -0.7 are suitable for most mooring line analyses. In the present study, a default value of -0.5 is used.

2.4.

The PEM which is a QS mooring line model was implemented by the research group of the authors (Cheng et al., 2019). Two coordinate systems including global and local ones are defined for each mooring line in PEM as shown in Fig. 4. The origin of the local system O' - $x'y'z'$ locates at the fairlead throughout, and the $x'y'$ plane is defined by instantaneous mooring line orientation. The local reference system can be obtained by moving the global system to the fairlead and rotating by θ angle to follow the mooring line plane. The mooring line is discretized into a series of segments, over which equations of static equilibrium in horizontal and vertical directions are established as (see Fig. 5)

$$T_x^{i+1} = T_x^i + D^i ds\sin\varphi^{i+1} + F^i ds\cos\varphi^{i+1} \tag{68}$$

$$T_z^{i+1} = T_z^i - D^i ds\cos\varphi^{i+1} + F^i ds\sin\varphi^{i+1} + w^i dl \tag{69}$$

where T_x and T_z are horizontal and vertical components of the mooring line tension, respectively; φ is the angle of the tension vector with respect to the horizontal plane; w is the net weight of mooring line in water per unit length; D and F are normal and tangential components of the drag, respectively; and the subscript i means the ith node at start
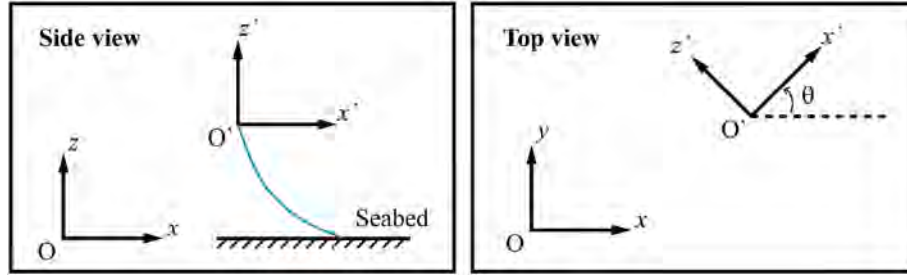
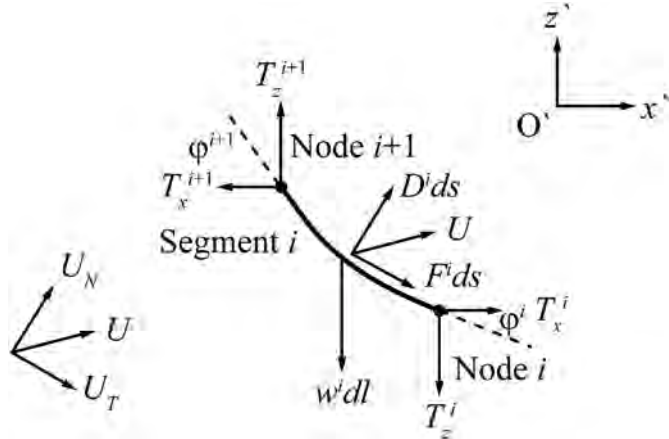**Fig. 4.** Coordinate systems of a mooring line in the PEM mooring line model.

Fig. 5. Force analysis of a mooring line segment in the PEM mooring line model.

point of the ith line segment. Dl and ds are the segment lengths before and after elongation respectively, and they are related by the line tension as

$$ds = \left(1 + \frac{T^{i+1}}{EA}\right)dl \tag{70}$$

The secant method in an iterative manner is executed as shown by Fig. 6. In each iteration, the extrapolating step proceeds from the fairlead to the anchor, and the extrapolated anchor is compared to the actual one by the coordinates. The iteration converges when the error in anchor location is less than a preset value. If the test fails, a new iteration starts to correct the mooring line solution based on the error in the previous iteration. To demonstrate the correction process, the following relations are defined.

$$x_0^{'k} = f\left(T_{xn}^k, T_{zn}^k\right) \tag{71}$$

$$z_0^{'k} = g\left(T_{xn}^k, T_{zn}^k\right) \tag{72}$$

$$X_0' = f(T_{xn}, T_{zn}) \tag{73}$$

$$Z_0' = g(T_{xn}, T_{zn}) \tag{74}$$

where f and g functions represent the extrapolating step to predict the x and y coordinates of the anchor in the local system, respectively. X_0' and $z_0^{'k}$ are the extrapolated anchor coordinates in the kth iteration while X_0' and Z_0' are the actual anchor coordinates. T_{xn}^k and T_{zn}^k are the fairlead tension predictions in the kth iteration while T_{xn}^k and T_{zn}^k are the real fairlead tension solutions. The errors in coordinates are calculated as

$$e_x^k = X_0' - x_0^{'k} \tag{75}$$
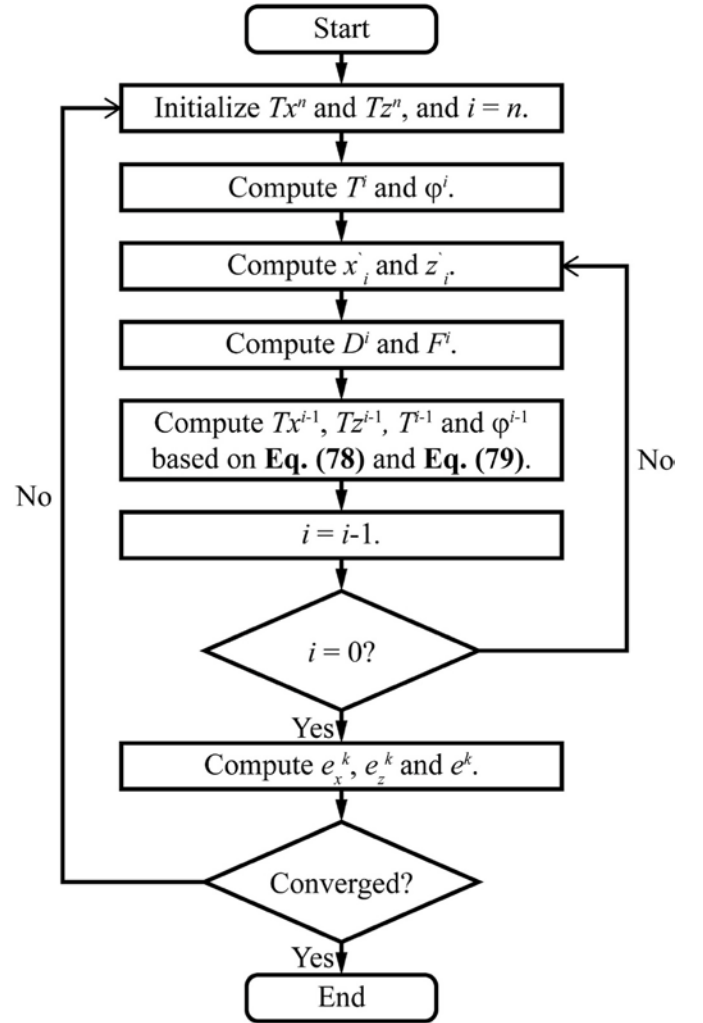
Fig. 6. Schematic of the iterative algorithm in the PEM mooring line model.

$$e_z^k = Z_0' - z_0^{'k} \tag{76}$$

$$e^k = \sqrt{\left(X_{err}^k\right)^2 + \left(Z_{err}^k\right)^2} \tag{77}$$

Rewriting Eq. (73) and Eq. (74) using the extrapolated fairlead tensions in the kth iteration with the Taylor expansion ignoring high order terms and doing some manipulations, the fairlead tension correction equations are obtained as follows.

$$T_{xn}^{k+1} = T_{xn}^k + \left[\left(e_x^k\frac{\partial g}{\partial T_{zn}} - e_z^k\frac{\partial f}{\partial T_{zn}}\right) \bigg/ \left(\frac{\partial f}{\partial T_{xn}}\frac{\partial g}{\partial T_{zn}} - \frac{\partial f}{\partial T_{zn}}\frac{\partial g}{\partial T_{xn}}\right)\right]_{\left(T_{xn}^k, T_{zn}^k\right)} \tag{78}$$

$$T_{zn}^{k+1} = T_{zn}^k + \left[\left(e_z^k \frac{\partial f}{\partial T_{xn}} - e_x^k \frac{\partial g}{\partial T_{xn}} \right) \Big/ \left(\frac{\partial f}{\partial T_{xn}} \frac{\partial g}{\partial T_{zn}} - \frac{\partial f}{\partial T_{zn}} \frac{\partial g}{\partial T_{xn}} \right) \right]_{\left(T_{xn}^k, T_{zn}^k \right)} \quad (79)$$

To obtain the four partial derivatives in Eq. (78) and Eq. (79), the extrapolated mooring line results in the k-1st iteration are used as follows. Note that the approximations in Eq. (81) and Eq. (83) help reduce the number of extrapolating loops by one in each iteration without affecting the final predictions.

$$\frac{\partial f}{\partial T_{xn}} \bigg|_{\left(T_{xn}^k, T_{zn}^k \right)} = \frac{f\left(T_{xn}^k, T_{zn}^k \right) - f\left(T_{xn}^{k-1}, T_{zn}^k \right)}{T_{xn}^k - T_{xn}^{k-1}} \quad (80)$$

$$\frac{\partial f}{\partial T_{zn}} \bigg|_{\left(T_{xn}^k, T_{zn}^k \right)} = \frac{f\left(T_{xn}^k, T_{zn}^k \right) - f\left(T_{xn}^k, T_{zn}^{k-1} \right)}{T_{zn}^k - T_{zn}^{k-1}} \approx \frac{f\left(T_{xn}^{k-1}, T_{zn}^k \right) - f\left(T_{xn}^{k-1}, T_{zn}^{k-1} \right)}{T_{zn}^k - T_{zn}^{k-1}} \quad (81)$$

$$\frac{\partial g}{\partial T_{xn}} \bigg|_{\left(T_{xn}^k, T_{zn}^k \right)} = \frac{g\left(T_{xn}^k, T_{zn}^k \right) - g\left(T_{xn}^{k-1}, T_{zn}^k \right)}{T_{xn}^k - T_{xn}^{k-1}} \quad (82)$$

$$\frac{\partial g}{\partial T_{zn}} \bigg|_{\left(T_{xn}^k, T_{zn}^k \right)} = \frac{g\left(T_{xn}^k, T_{zn}^k \right) - g\left(T_{xn}^k, T_{zn}^{k-1} \right)}{T_{zn}^k - T_{zn}^{k-1}} \approx \frac{g\left(T_{xn}^{k-1}, T_{zn}^k \right) - g\left(T_{xn}^{k-1}, T_{zn}^{k-1} \right)}{T_{zn}^k - T_{zn}^{k-1}} \quad (83)$$

2.5. Catenary

The analytical catenary mooring line model of QS nature by the research group of the authors is used. The model is capable of solving mooring lines of catenary shape with parts lied on the ground, but extension in line is omitted. A schematic of the model is shown in Fig. 7. In the figure, X and H are the horizontal and vertical distances between the anchor and the fairlead respectively, and L is the constant length of the line. Position P is the tangent point between the line and the ground, and is the origin of the coordinate system P-xz of the instantaneous mooring line. The length of the line lying on the ground is denoted as p while the length of the portion forming the catenary shape is denoted as q. Analytical solution to the mooring line shown in Fig. 7 is given as

$$z = \begin{cases} a\left(\cosh \frac{x}{a} - 1 \right) & 0 \leq x \leq X - p \\ 0 & -p \leq x < 0 \end{cases} \quad (84)$$

Where a ($= T_h/w$) is the catenary parameter, T_h is the horizontal tension at any section, and w is the net weight of mooring line in water per unit length. The two unknowns a and p are calculated by the following equations.

$$a = \frac{(L-p)^2 - H^2}{2H} \quad (85)$$

$$e^{\left[(X-p) \cdot \frac{2H}{(L-p)^2 - H^2} \right]} - \frac{2H}{L-p-H} - 1 = 0 \quad (86)$$
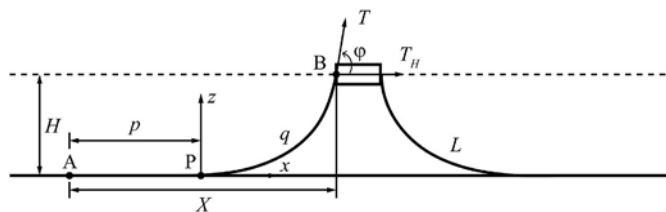
2.6. QS

The QS mooring line model of MAP developed by Masciola et al. (2013a) is used. The model is similar to the catenary model in section 2.5 but line extension is allowed herein. The reference frame and relevant entities of the model are plotted in Fig. 8. The analytical solutions for the mooring line with parts lying on the ground are given as

$$x(s) = \begin{cases} s & 0 \leq s \leq \gamma \\ s + \frac{C_B w}{2EA} \left[s^2 - 2s\gamma + \gamma\lambda \right] & \gamma \leq s \leq L_B \\ L_B + \frac{H}{w} \sinh^{-1}\left[\frac{w(s-L_B)}{H} \right] + \frac{Hs}{EA} + \frac{C_B w}{2EA}\left[\gamma\lambda - L_B^2 \right] & L_B \leq s \leq L \end{cases} \quad (87)$$

$$z(s) = \begin{cases} 0 & 0 \leq s \leq L_B \\ \frac{H}{w}\left\{ \sqrt{1 + \left[\frac{w(s-L_B)}{H} \right]^2} - 1 \right\} + \frac{w(s-L_B)^2}{2EA} & L_B \leq s \leq L \end{cases} \quad (88)$$

$$T(s) = \begin{cases} \max[H + C_B w(s-L_B), 0] & 0 \leq s \leq L_B \\ \sqrt{H^2 + [w(s-L_B)]^2} & L_B \leq s \leq L \end{cases} \quad (89)$$

where s denotes the length along the unstretched line; w is the net weight of mooring line in water per unit length; EA represents the extensional stiffness; L_B is the length of the line lying on the ground; C_B is the friction coefficient of the line-seabed contact; γ and λ are defined as follows.

$$\gamma = L_B - \frac{H}{C_B w} \quad (90)$$

$$\lambda = \begin{cases} \gamma & if\ \gamma > 0 \\ 0 & otherwise \end{cases} \quad (91)$$

3. Dynamics of catenary cable due to fairlead excitation

3.1. Problem description

The cable experiments from Azcona et al. (2017) are used for the comparison of the three dynamic mooring models. Fig. 9 illustrates the configuration of the experiments. As is shown, the wave tank having a size of 50m × 30m × 5 m gives the depth of 5 m in all the tests. The chain line submerged in the water with an initial catenary shape is actuated at the top suspension point into a sinusoidal horizontal motion in the plane of the cable. The properties of the chain line are given in Table 1, and the parameters used in the tests are presented in Table 2. The chain model properties are resulted by a scale of 1/40, and the 5 m depth basin corresponds to a 200 m depth sea and the full-scale line properties are close to the OC4 FOWT mooring lines (Robertson et al., 2014a). Two
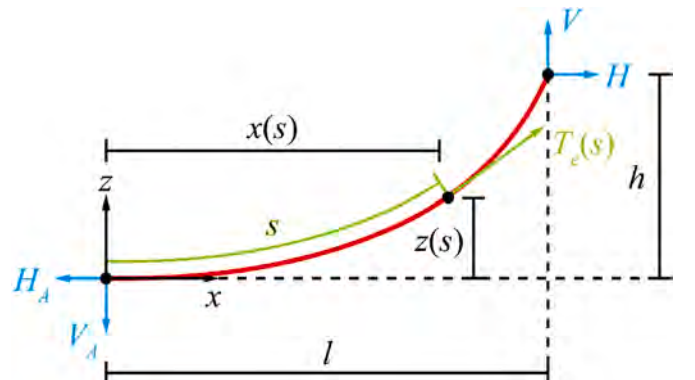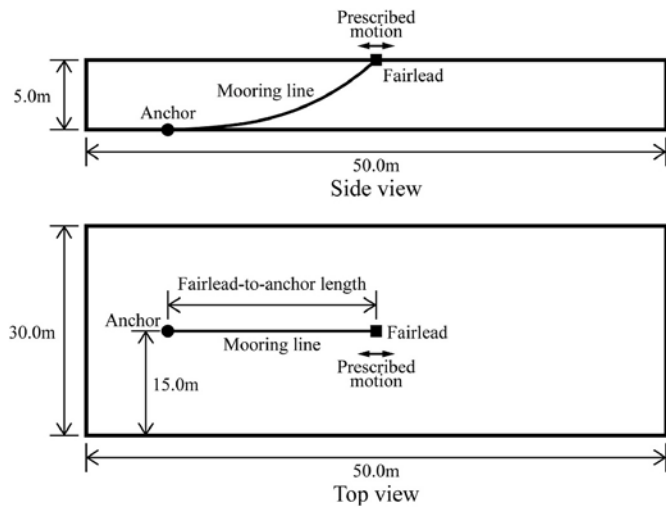
Fig. 7. Schematic of the catenary mooring line model.

Fig. 8. Schematic of the QS mooring line model.

Fig. 9. Configuration of the catenary cable experiments.

Table 1
Properties of the mooring line.

Parameters	Values
Unstretched length	21 m
Mass per unit length	0.069 kg/m
Line density	7850 kg/m^3
Axial stiffness	3.416E5 N
Coefficient for the structural Rayleigh damping	0.0001
Equivalent hydrodynamic diameter	0.0034 m
Added mass coefficient	1.0
Normal drag coefficient	1.4
Tangential drag coefficient	0.67

Table 2
Parameters used in the experimental tests.

Cases	d	Type	Amplitude	Period
1	19.364	Static	/	/
2	19.872	Static	/	/
3	19.364	Dynamic	0.25 m	1.58 s
4	19.364	Dynamic	0.25 m	3.16 s
5	19.364	Dynamic	0.25 m	4.74 s
6	19.872	Dynamic	0.25 m	1.58 s
7	19.872	Dynamic	0.25 m	3.16 s
8	19.872	Dynamic	0.25 m	4.74 s

configurations of lines are used, i.e., chains with fairlead-to-anchor distances of 19.364 m and 19.872 m. For each chain, both static and dynamic analyses are conducted. In the dynamic cases, three periods, i.e., 1.58s, 3.16s and 4.74s, are used, which correspond to the oscillation periods of 10s, 20s and 30s in full scale, respectively. The amplitude of the forced motions is fixed at 0.25 m, which is 10 m in full scale. Moreover, in the tests, 8 markers located successively along the chain

Table 3
Position of the markers along the chain line.

Markers	Position along the chain line from fairlead
1	0.656 m
2	1.155 m
3	1.655 m
4	2.149 m
5	2.646 m
6	3.152 m
7	3.655 m
8	4.164 m

line are used to measure the motion. As is shown in Table 3, the gap between adjacent markers along the chain line is approximately 0.5 m.

3.2. Simulation details

The dynamic mooring line models of LDG FEM (Palm et al., 2017), LM (Hall and Goupee, 2015) and FDM (Chen et al., 2018) are compared. The numerical settings are almost the same as the experiments except minor differences in cable and seabed contact models due to different capabilities of the codes. In specific, only axial stiffness of the cable is considered in LDG FEM and LM while axial, bending and torsional stiffness are implemented in FDM. For the seabed contact, both vertical reaction force and horizontal friction between mooring and seabed are considered in LDG FEM while only vertical force is computed in LM and FDM. Note that the oscillation of cable tension observed under snap load conditions is claimed to be related to the ignorance of horizontal seabed friction in Azcona et al. (2017). This is further discussed in this study. Table 4 shows the parameters used in the line-seabed contact model.

A convergence study for the three models is conducted with the test cases 3 and 6. For each test, three numbers of segments, i.e., 28, 42 and 60, are used. It is found that the cable discretized into 42 elements is sufficient for accurate numerical computation.

3.3. Static cases

The static cases 1 and 2 in Table 2 are simulated by LDG FEM, LM and FDM, and the results are compared to the data of Azcona et al. (2017) in Fig. 10. It is seen that for both line configurations, the experimental and numerical results agree well, confirming the reliability of the models in computing the static catenary shape of mooring lines and thus providing accurate initial mooring states for dynamic analysis. A quantitative comparison of the fairlead tension is presented in Table 5. It is shown that the present results are in accordance with the experimental and numerical results in Azcona et al. (2017). The LDG FEM and FDM give the same fairlead tension in both line configurations. The maximum relative differences to the measured data for test cases 1 and 2 are 0.37% and 2.62% respectively and occur both by LM.

3.4. Dynamics cases

The present predicted fairlead tensions of dynamic cases are compared to the measured and simulated data from Azcona et al. (2017) in Fig. 11. The numerical tool used in Azcona et al. (2017) is a LM formulation. The figure shows the tension at the mooring fairlead against the fairlead displacement, and the data is plotted after the steady state has been reached.

As seen in Fig. 11(c)–(d), the agreement of the LDG FEM, LM and FDM results with the experimental data is all good when the excitation periods are 3.16s and 4.74s. The LDG FEM appears to be the best among the three models as it follows closely the fairlead tension variation of both the experimental and numerical results (Azcona et al., 2017). Note that these two periods of excited mooring motion correspond to the harmonic condition described in Suhara et al. (1981), where the fairlead tension varies sinusoidally in the time domain. For the excitation period of 1.58s, Fig. 11(a) and (b) show that the best match to the experimental and numerical data over the whole cycle is the LDG FEM model while the LM and FDM give evidently higher predictions when the fairlead moves away from the anchor. The dynamic cases with this period are the

Table 4
Characteristics of the line-seabed contact and friction models.

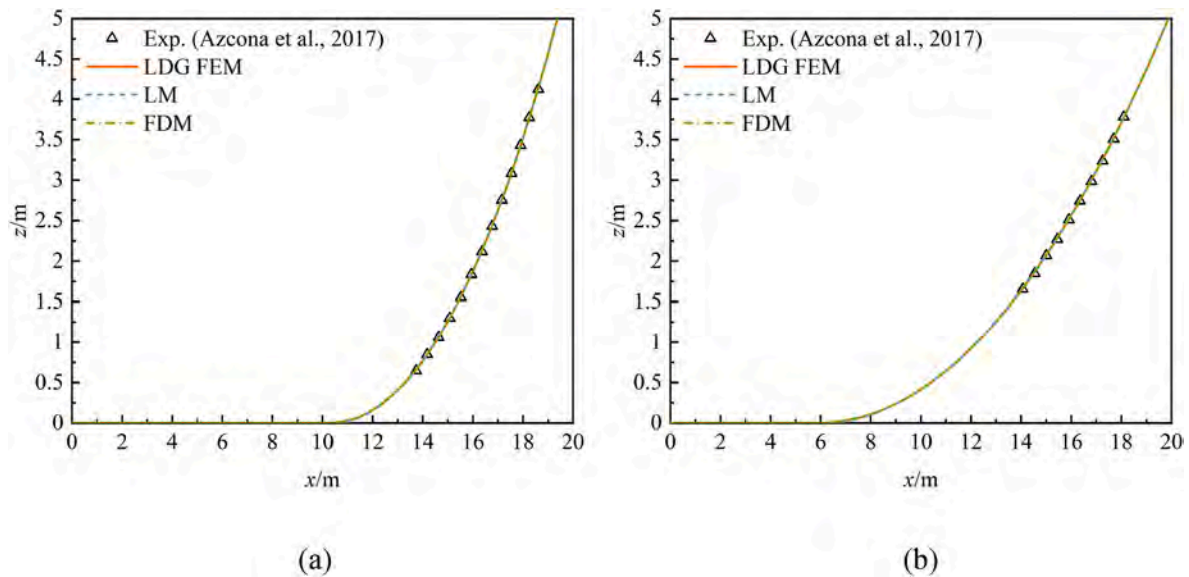| Parameters	Values
Vertical seabed stiffness	5.882E3 N/m^3
Vertical seabed damping	2.941E1 Ns/m^3
Friction coefficient	0.5

Fig. 10. Comparison of static catenary mooring line shape for (a) test case 1 and (b) test case 2.

Table 5
Comparison of static catenary mooring line fairlead tension for test case 1 and 2.

Methods	Test case 1	Test case 2
Exp. (Azcona et al., 2017)	8.13 N	14.48 N
LM (Azcona et al., 2017)	8.10 N	14.70 N
LDG FEM	8.14 N	14.82 N
LM	8.10 N	14.86 N
FDM	8.14 N	14.82 N

most challenging ones among the tests as the mooring line undergo the snap condition in each excitation loop (Suhara et al., 1981). As displayed by the measurements in the two plots, the mooring line with a fairlead-to-anchor distance of 19.364 m partially loses tension when the fairlead moves towards the anchor, while for the mooring line with a fairlead-to-anchor distance of 19.872 m, the fairlead tension entirely loses during the same process and approximates zero over half of the oscillation period. The sudden snap load after the slack state poses difficulties for accurate modeling of mooring dynamics. It is observed in Fig. 11(a) and (b) that the most discrepancies of fairlead tension for LM and FDM occur approximately at the time when the fairlead departs from the anchor with the maximum velocity.

One thing worth noting is that as indicated by the experimental data for case 6 in Fig. 11(b), when the chain fairlead starts reversing motion from approaching the anchor, the mooring line that falls freely is abruptly pulled tight producing a snap load, i.e., a sharp increase in the internal tension, and during the recovery process, the fairlead tension experiences a plateau before again ascending to peak value. This tension variation course is roughly captured by the LM model in Azcona et al. (2017), but the tension plateau is largely smeared with the starting point advanced. The same effect occurs for the numerical models in the present study. Moreover, fairlead tension fluctuation emerges during the recovery period for the LDG FEM formulation which exhibits the best reliability with regards to measurements at all other moments. The similar fluctuation has also been observed for the numerical tool used in Azcona et al. (2017), and was claimed to be related to the omission of seabed friction in the dynamic mooring modeling. In order to boost the account, Azcona et al. (2017) applied both the seabed friction model in OPASS and the seabed damping model in 3DFloat to the mooring line dynamics. It was asserted in Azcona et al. (2017) that the friction or damping from the seabed takes effect on mooring line segments resting on the seabed such that small motions of these segments and thus

tension fluctuations are avoided during the tension-less period of the dynamic loop. In other words, the horizontal reaction force from the seabed acts as a mitigating mechanism to damp out the unphysical high frequency fluctuations. Nevertheless, the present LDG FEM results plotted in Fig. 11(b) are obtained with the seabed friction model switched on and set up according to Table 4. It should be pointed out that slight fairlead tension fluctuations occur occasionally during the excitation loop for the LDG FEM in all the dynamic cases as seen in Fig. 11. It is guessed that the dramatic tension fluctuations during the slack-snap process of the high frequency excitation test case 6 are attributed to the inherent capability of the model. In addition, the LM and FDM methods which possess only spring-damper mooring-seabed contact model show no fluctuations in the sharp tension recovery. The assertation on the causes for the unphysical high frequency tension fluctuations in Azcona et al. (2017) may not apply to the LM and FDM models used in the present study. It is suspected by the authors that as the axial damping on a chain line can effect from seabed friction, tangential drag and internal damping, the latter two factors may contribute to the suppression of high frequency oscillation for LM and FDM.

Figs. 12–17 show the comparison of trajectory of markers (see Table 3) along the mooring line for test cases 3–8, respectively. In each figure, motion results of makers 1–8 are presented in sub-figures. Experimental and numerical results from Azcona et al. (2017) are also included. The scale and length of both the x and z axis are the same in all plots to provide a convenient visual comparison for all makers.

It is seen in the six figures that the motion of the mooring line markers is majorly horizontal in positions near the fairlead and transforms to a vertical manner away from the fairlead. Figs. 12–14 and 16–17 indicate that the agreement of the numerical results obtained by LDG FEM, LM and FDM to the measured data is very good, and the most promising mooring dynamics model appears to be LDG FEM which is consistent with the observations on Fig. 11. In specific, the predicted marker motions by LDG FEM show the closest match to measurements in the figures while both LM and FDM show slight deviations during one loop of excitation. For the test case 6 shown in Fig. 15 where the mooring line with a fairlead-to-anchor distance of 19.872 m is excited with a period of 1.58s, a considerable shift of the marker motion is observed for the results obtained by FDM, and only LDG FEM gives satisfactory predictions. This is consistent with the fairlead tension shift for FDM in Fig. 11(b). Also note that for this most challenging test case, the markers located deep into the water experience a complex motion
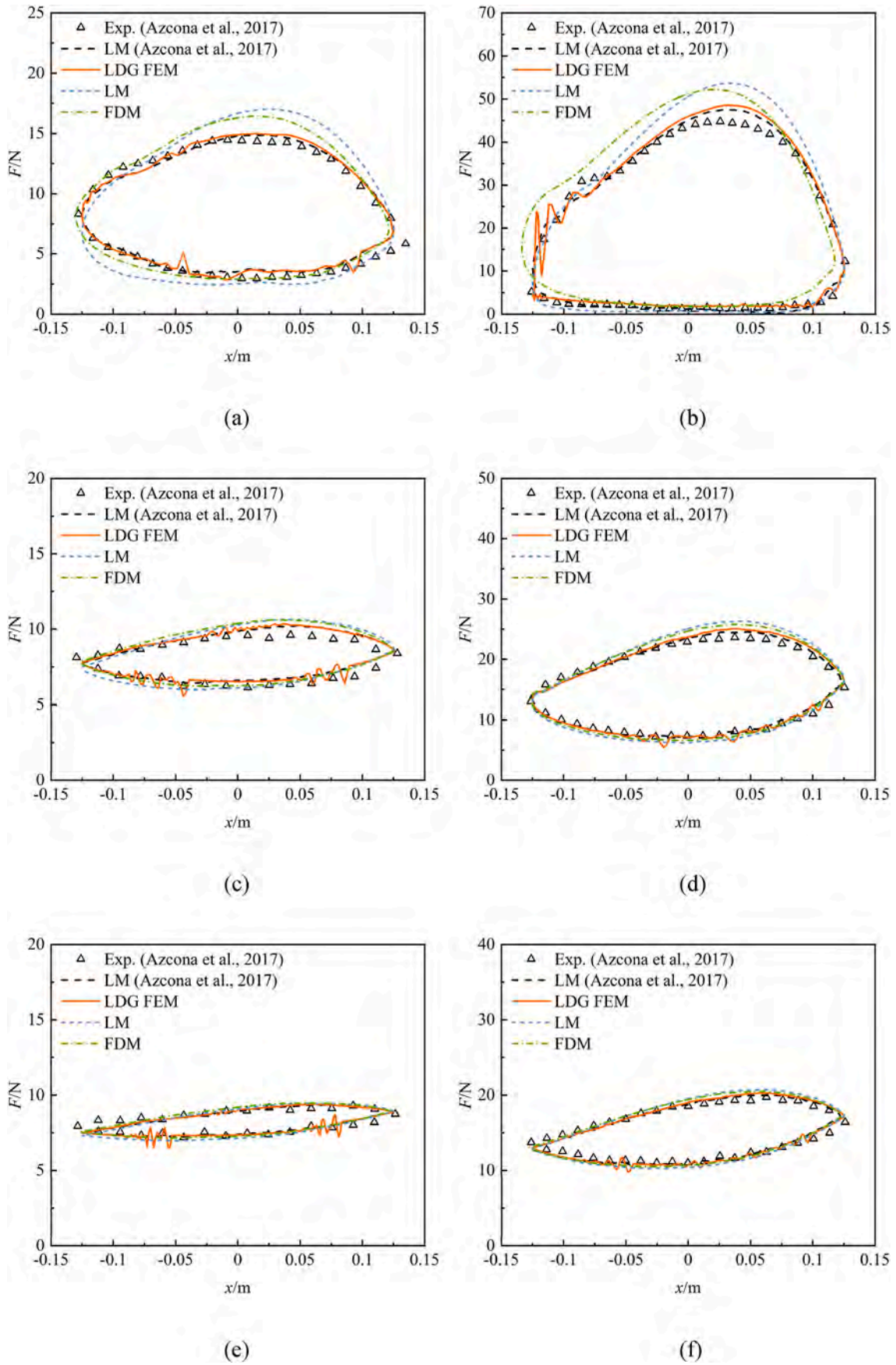
Fig. 11. Comparison of fairlead tension for (a) test case 3, (b) test case 6, (c) test case 4, (d) test case 7, (e) test case 5, and (f) test case 8.
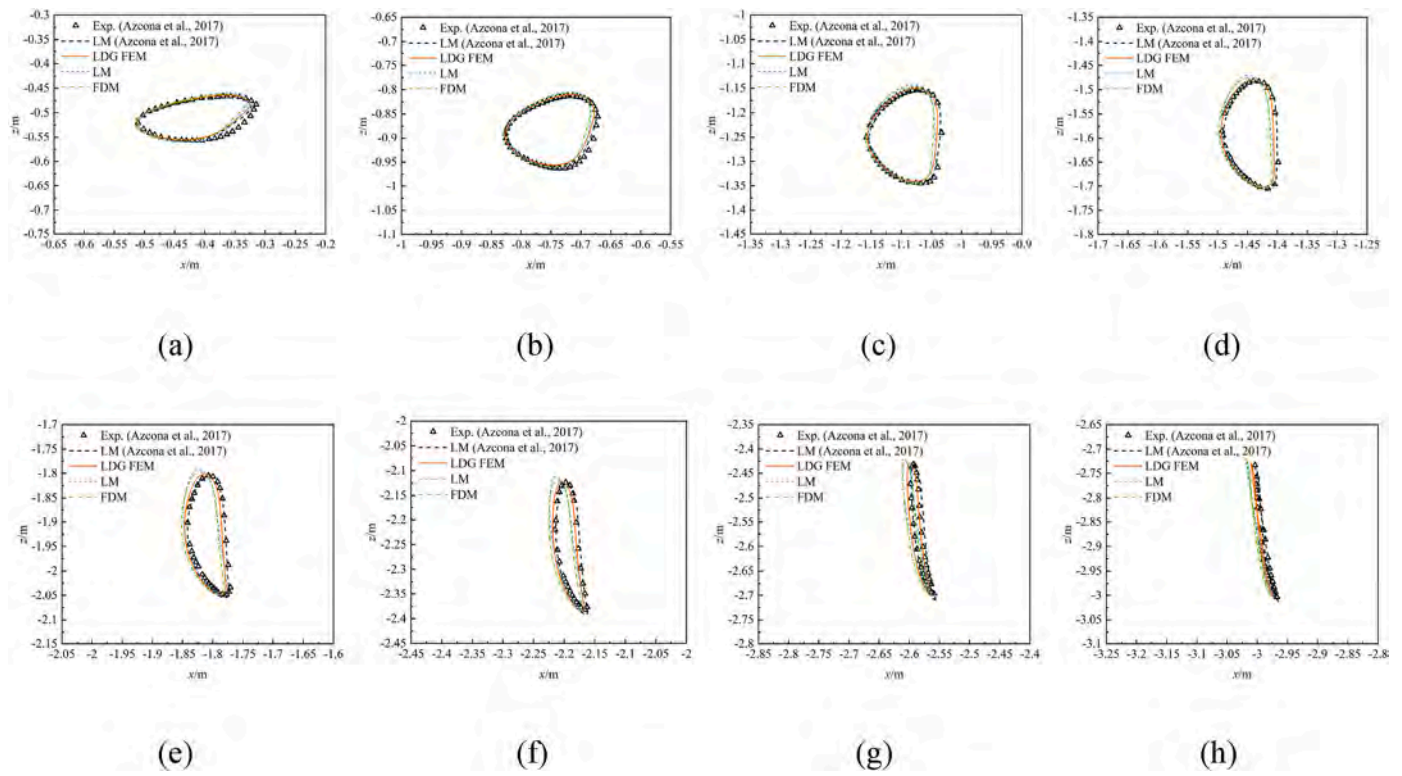
Fig. 12. Comparison of trajectory described by (a) marker 1, (b) marker 2, (c) marker 3, (d) marker 4, (e) marker 5, (f) marker 6, (g) marker 7, and (h) marker 8 for test case 3.
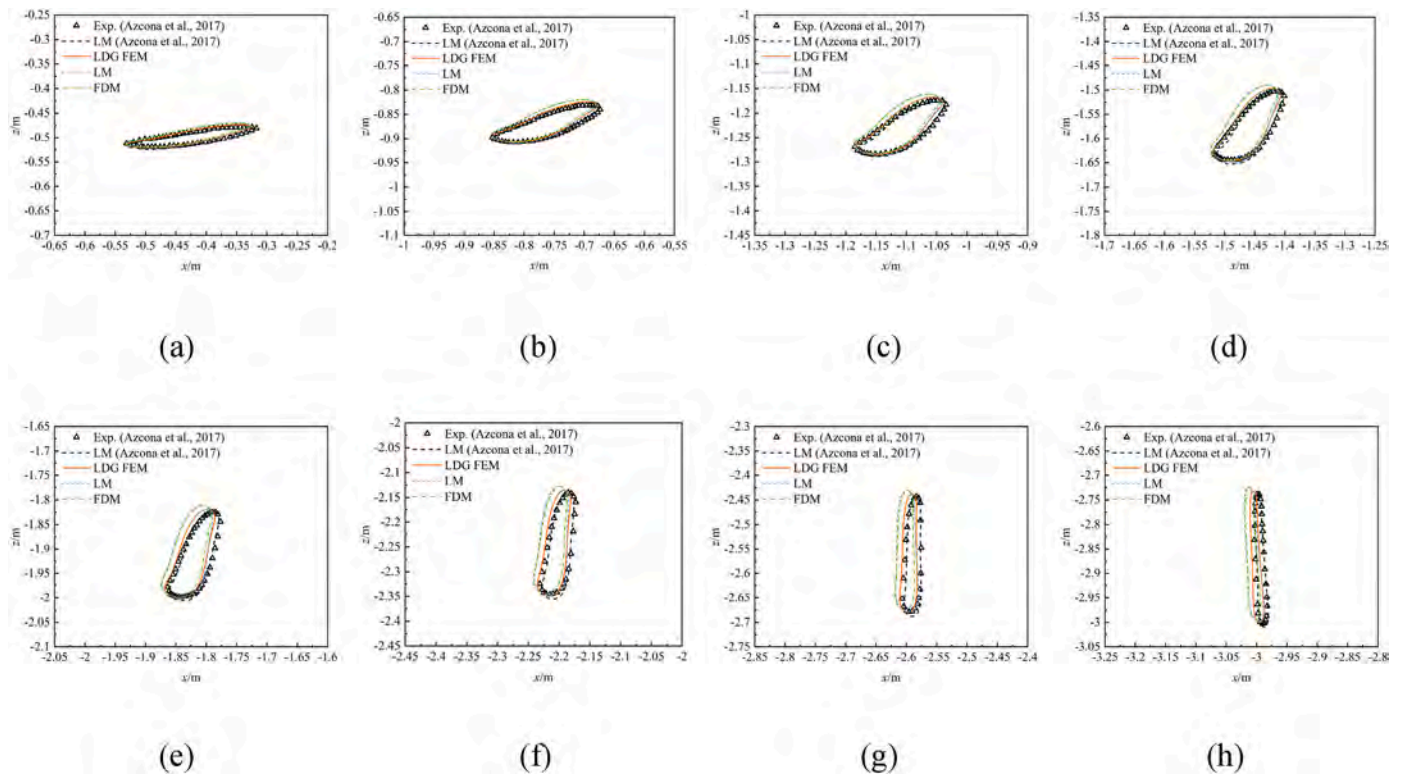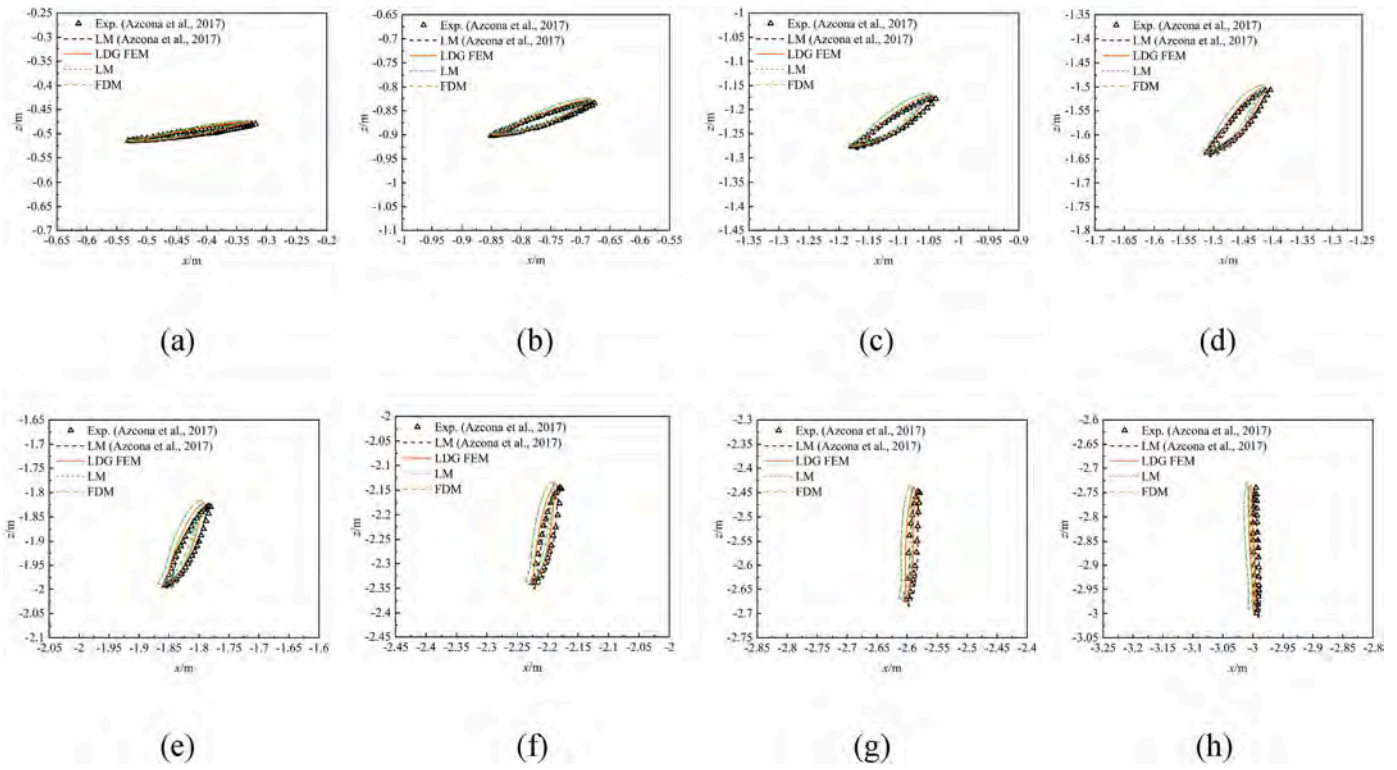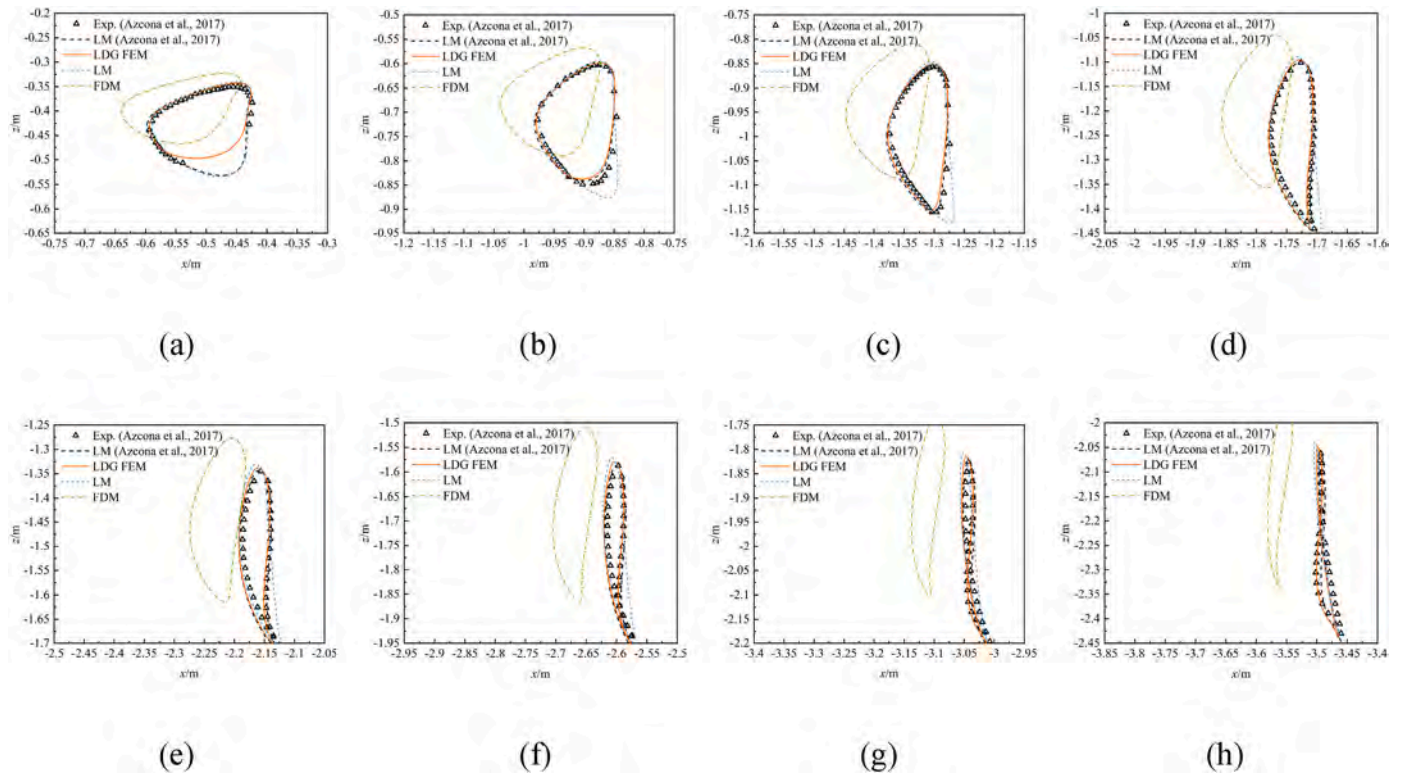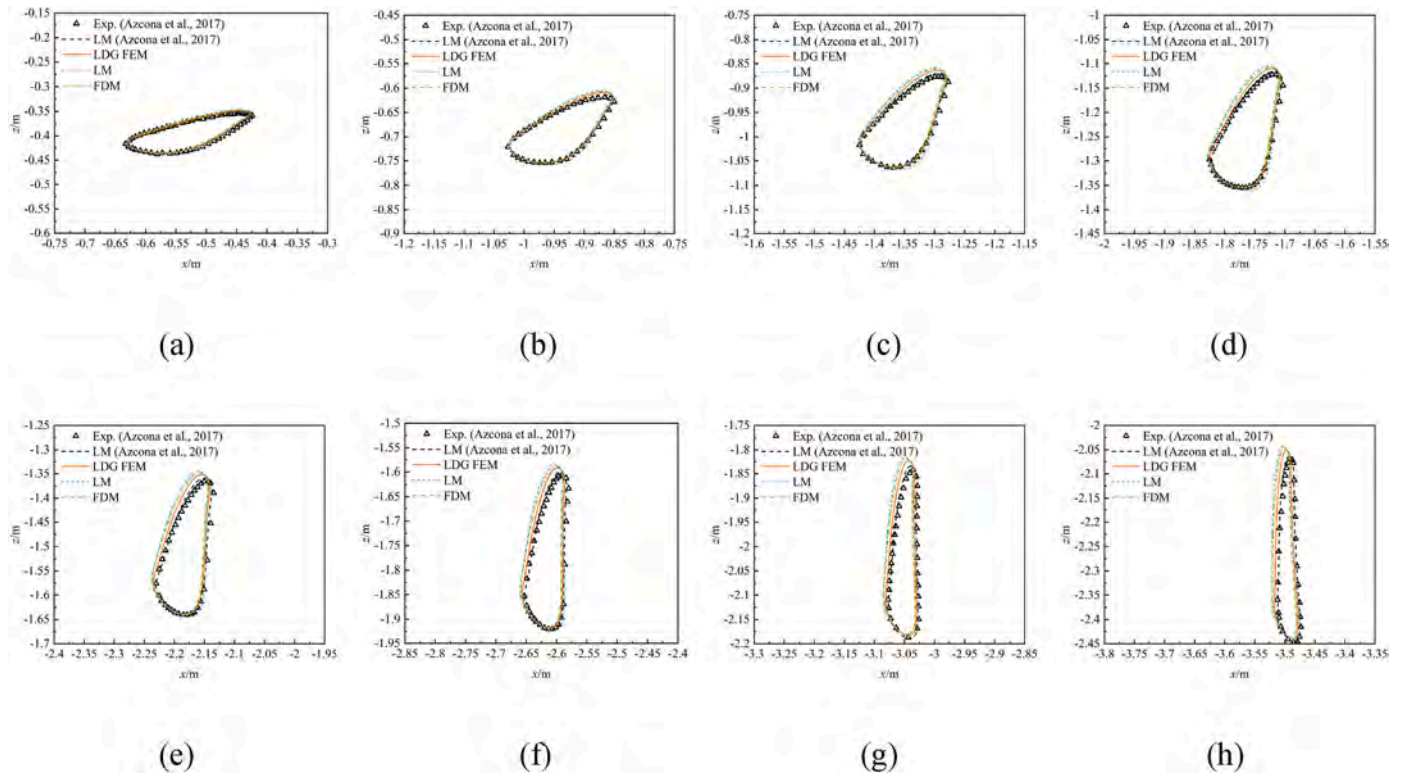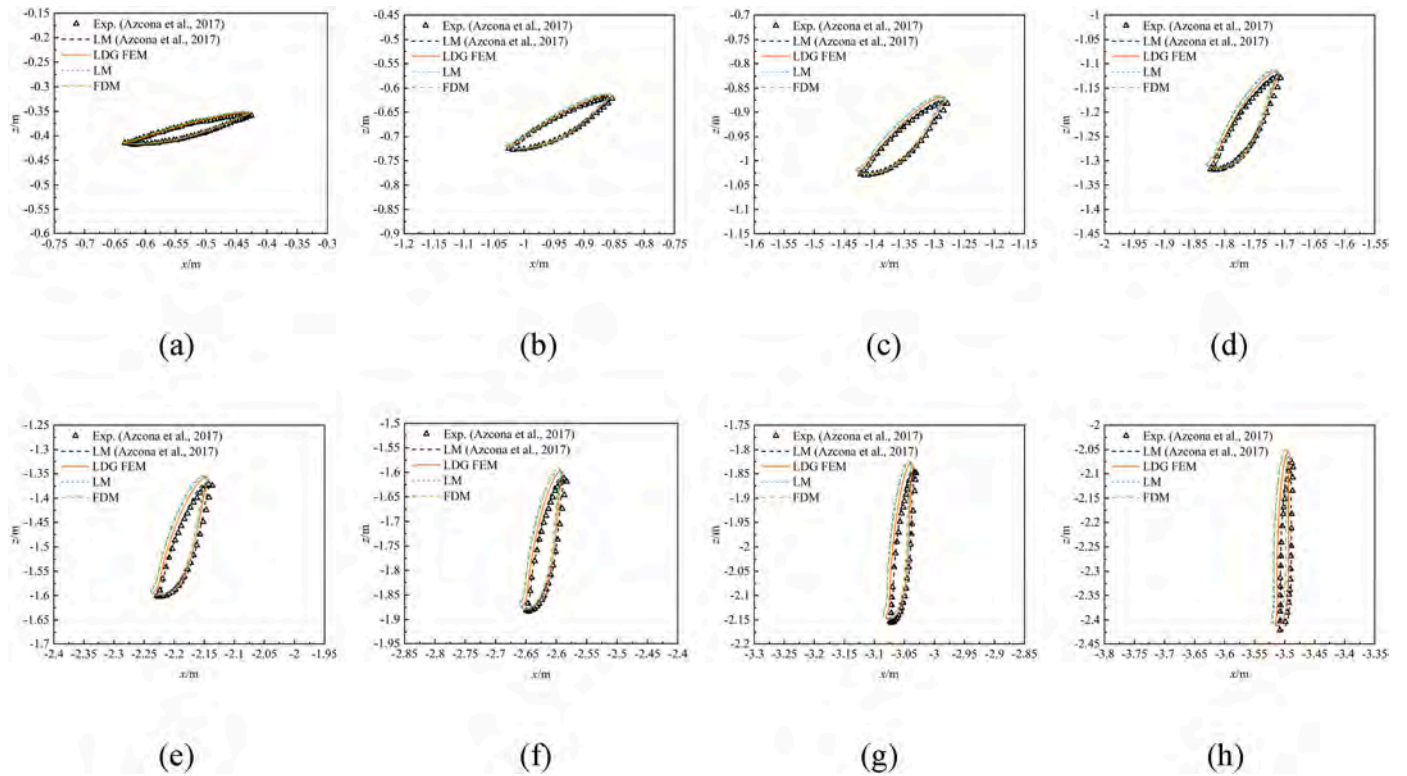

Fig. 13. Comparison of trajectory described by (a) marker 1, (b) marker 2, (c) marker 3, (d) marker 4, (e) marker 5, (f) marker 6, (g) marker 7, and (h) marker 8 for test case 4.

Fig. 14. Comparison of trajectory described by (a) marker 1, (b) marker 2, (c) marker 3, (d) marker 4, (e) marker 5, (f) marker 6, (g) marker 7, and (h) marker 8 for test case 5.

Fig. 15. Comparison of trajectory described by (a) marker 1, (b) marker 2, (c) marker 3, (d) marker 4, (e) marker 5, (f) marker 6, (g) marker 7, and (h) marker 8 for test case 6.

Fig. 16. Comparison of trajectory described by (a) marker 1, (b) marker 2, (c) marker 3, (d) marker 4, (e) marker 5, (f) marker 6, (g) marker 7, and (h) marker 8 for test case 7.

Fig. 17. Comparison of trajectory described by (a) marker 1, (b) marker 2, (c) marker 3, (d) marker 4, (e) marker 5, (f) marker 6, (g) marker 7, and (h) marker 8 for test case 8.

behavior with the trajectory resembling the number "8" (See Fig. 15(g)–(h)). This movement results from the rapid loss and recovery of tension during the high frequency excitation motion. An interpretation for the occurrence of the complex marker motion is referred to Azcona et al. (2017). It is seen in Fig. 15(g)–(h) that the crossover motion of markers is well reproduced with the LDG FEM while the LM reduces the motion

$$x(t) = a\sin(2\pi ft)$$
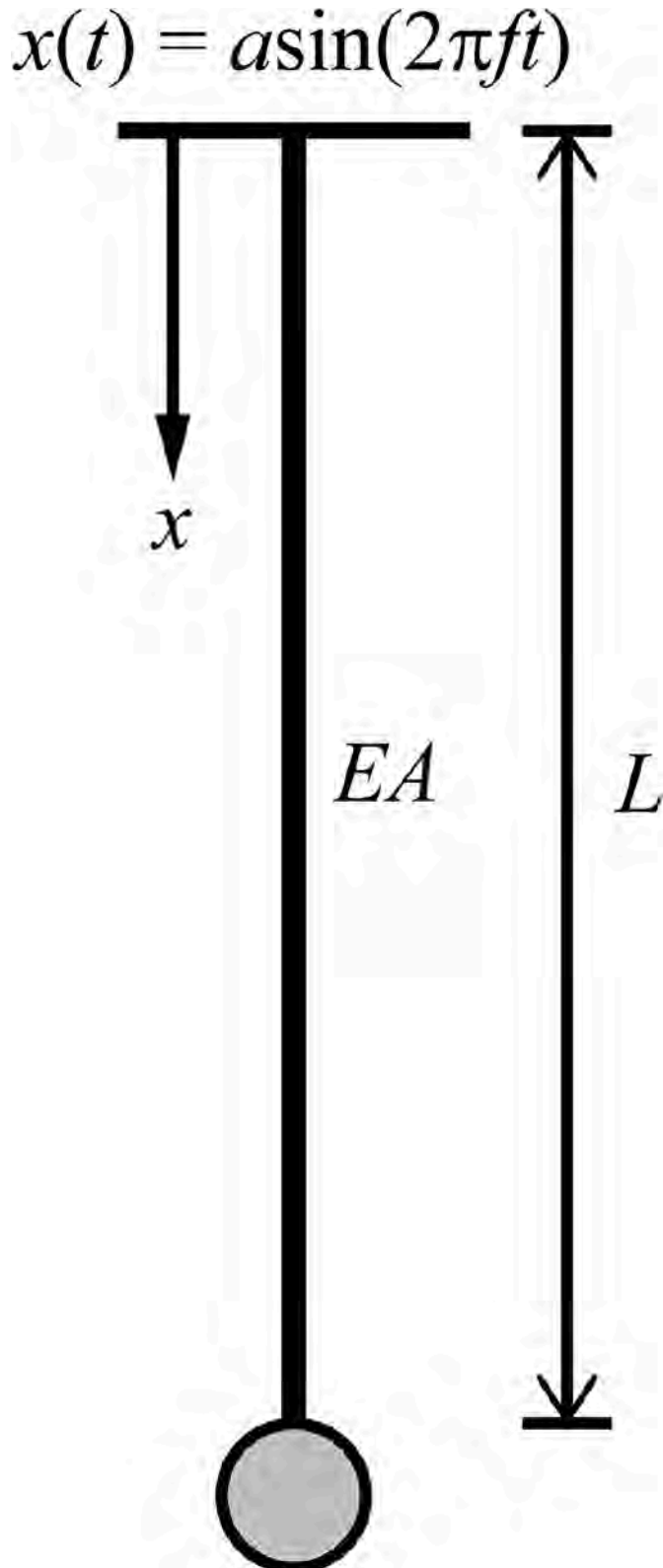
Fig. 18. Schematic of the hanging cable excited at upper end.

curve into a simply connected loop. Moreover, the LM gives strange marker motions during the free fall period as represented by the blue dashed curves in Fig. 15(a)–(c). It is suspected that the inferiority of the LM formulation for high frequency motions may result from the simplification of the mooring dynamics into concentrated mass linked with spring and damper.

4. Dynamics of hanging cable under axial excitation

4.1. Hanging cable with payload

A hanging cable excited axially is simulated to assess the dynamic mooring models (Zhu, 2010). As shown in Fig. 18, the hanging cable attached with a spherical payload at the lower end is excited by a sinusoidal motion at the upper support. As expected, only axial response is aroused in the cable. Table 6 and Table 7 summarize the properties of the cable and the payload, respectively. Two cases with oscillation amplitude of 0.078 m and frequencies of 0.807 Hz and 1.270 Hz are analyzed. The simulated tension at the top end normalized by the static tension T_0 along with the experimental data from Zhu (2010) is shown in Fig. 19. Only results obtained by LDG FEM and LM are presented as the FDM lacks the functionality for concentrated mass. It is noted that the LDG FEM is used with the tangential drag coefficient of the cable raised to 1.0 since the simulation would crash with the original low value of 0.01. As seen in the figure, for the low frequency case, a harmonic tension variation is produced, and both LDG FEM and LM underestimate the amplitude of fluctuation with the LDG FEM predictions showing a better match to the experiments. For the high frequency case, snap loads occur as shown by the dark solid line in Fig. 19(b). The results obtained by LDG FEM show high frequency oscillations and are evidently low in peak tension. It is found that the result is closely related to the tangential drag coefficient in that a small value (e.g., 1.0) leads to a relatively large peak tension but with unphysical fluctuations while a large value suppresses the fluctuation but gives a further low peak tension. The internal damping, in contrast, appears to have insignificant effect on the stability and accuracy in this axial loading case. The results given by LM with normal setting of internal damping ratio $\xi = 1.0000$ considerably underpredict the tension and show a smooth variation. When the ratio is reduced to a very low value 0.0025 as Rodriguez Luis et al. (2020), the snap loading condition emerges.

Based on the analysis, it is concluded that for axial loading conditions, the damping along the cable line is essential for numerical stability. In LDG FEM, the internal damping mechanism is not sufficient for dissipating unphysical oscillations while damping from tangential drag is needed. In LM model, both internal damping and tangential drag contribute to eliminating high frequency oscillations. The difference can be explained by the formulation of the models (see Eq. (1) and Eq. (33)). As indicated by the equations, the internal damping force is directly acted on discretized nodes in LM and thus its effect on damping the motion is straight while in LDG FEM, the force from internal damping is added into the spatial term which is integrated over the element such that impacts from neighboring elements may counteract to reduce the effect.

Table 6
Properties of the hanging cable.

Parameters	Values
Unstretched length	18.9 m
Mass per unit length	0.0112 kg/m
Axial stiffness	1.342E5 N
Diameter	0.0016 m
Normal drag coefficient	1.2
Tangential drag coefficient	0.01

Table 7
Properties of the payload sphere.

Parameters	Values
Diameter	0.2032 m
Mass	12.2 kg
Added mass coefficient	0.18
Drag coefficient	0.5

4.2. Hanging cable without payload

To further examine the performance of the dynamic mooring models for axial excitation problems, a hanging cable without payload is considered. The test configuration is modified in that the lower end is kept fixed during the sinusoidal motion of the upper end. The same material property of the cable as that in section 4.1 is used. Two cases with oscillation amplitude of 0.078 m and frequencies of 0.807 Hz and 1.270 Hz are analyzed. S

It is found that the FDM fails for this problem. Tests indicate that the FDM seems to have a high requirement on the mooring line to be catenary. For the extreme case of a vertically placed cable, it fails to run. This may be due to the curvature terms in the governing equations which are closely connected with the shape of cable. For the other two models, the simulated tension at the top end normalized by the static tension T_0 is shown in Fig. 20. It is seen that in both cases, the two mooring models give identical results. It is also noted that changing the tangential drag coefficient has negligible effect on the LDG FEM predictions. This is in contrast to the case in section 4.1 where a free lower end with payload is

used. It implies that the axial damping mechanism is more effective when no free end exits in the mooring boundaries.

5. Hydrodynamics of a 15 MW semi-submersible FOWT under wave impacts

5.1. Physical model

To assess the mooring line models in CFD framework, the hydrodynamics of the UMaine VolturnUS-S semi-submersible platform under irregular and freak waves is simulated (Allen et al., 2020). This floater structure is designed for supporting the IEA 15 MW wind turbine which indicates the trend of large-scale wind turbines (Gaertner et al., 2020). As shown in Fig. 21, the reference platform consists of one main column on which the wind turbine tower is mounted, three offset columns radially placed surrounding the central tower, and three rectangular bottom pontoons connecting offset columns to the central one. The whole FOWT is deployed in a water depth of 200 m and the draft of the platform is 20 m under still water level (SWL). Three catenary mooring lines equally arranged around the platform is used for keeping the structure in place. Parameters of the FOWT system are depicted in Fig. 21 and the gross properties are presented in Table 8 and Table 9.

5.2. Numerical details

The numerical setup for the VolturnUS-S semi-submersible platform is shown in Fig. 22. The computational domain is sized to 900 m, 500 m
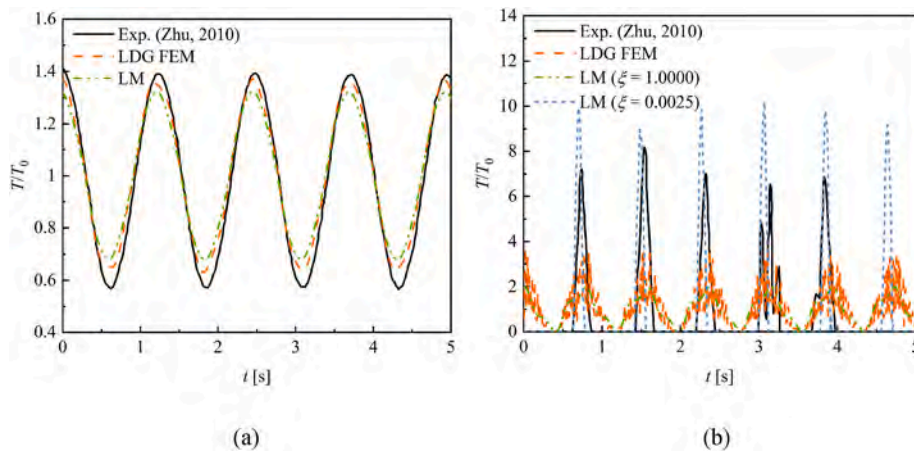

Fig. 19. Tension at the upper end of the hanging cable with payload: (a) $f = 0.807$ Hz; (b) $f = 1.270$ Hz.
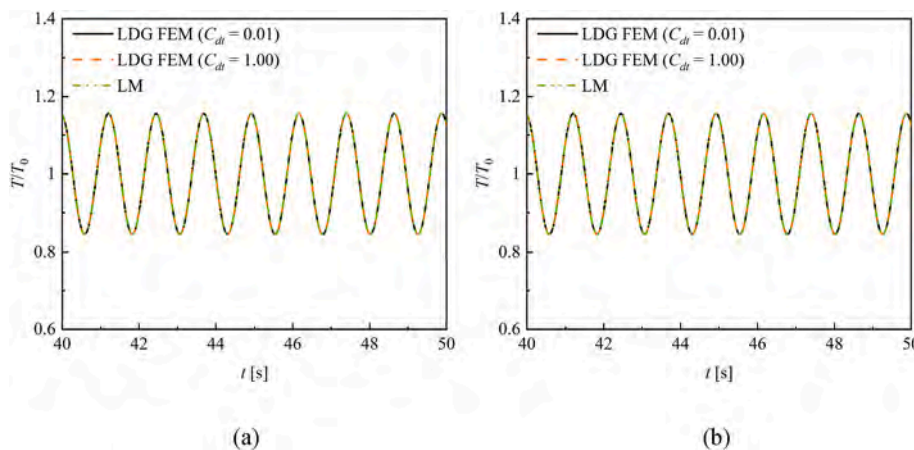

Fig. 20. Tension at the upper end of the hanging cable without payload: (a) $f = 0.807$ Hz; (b) $f = 1.270$ Hz.
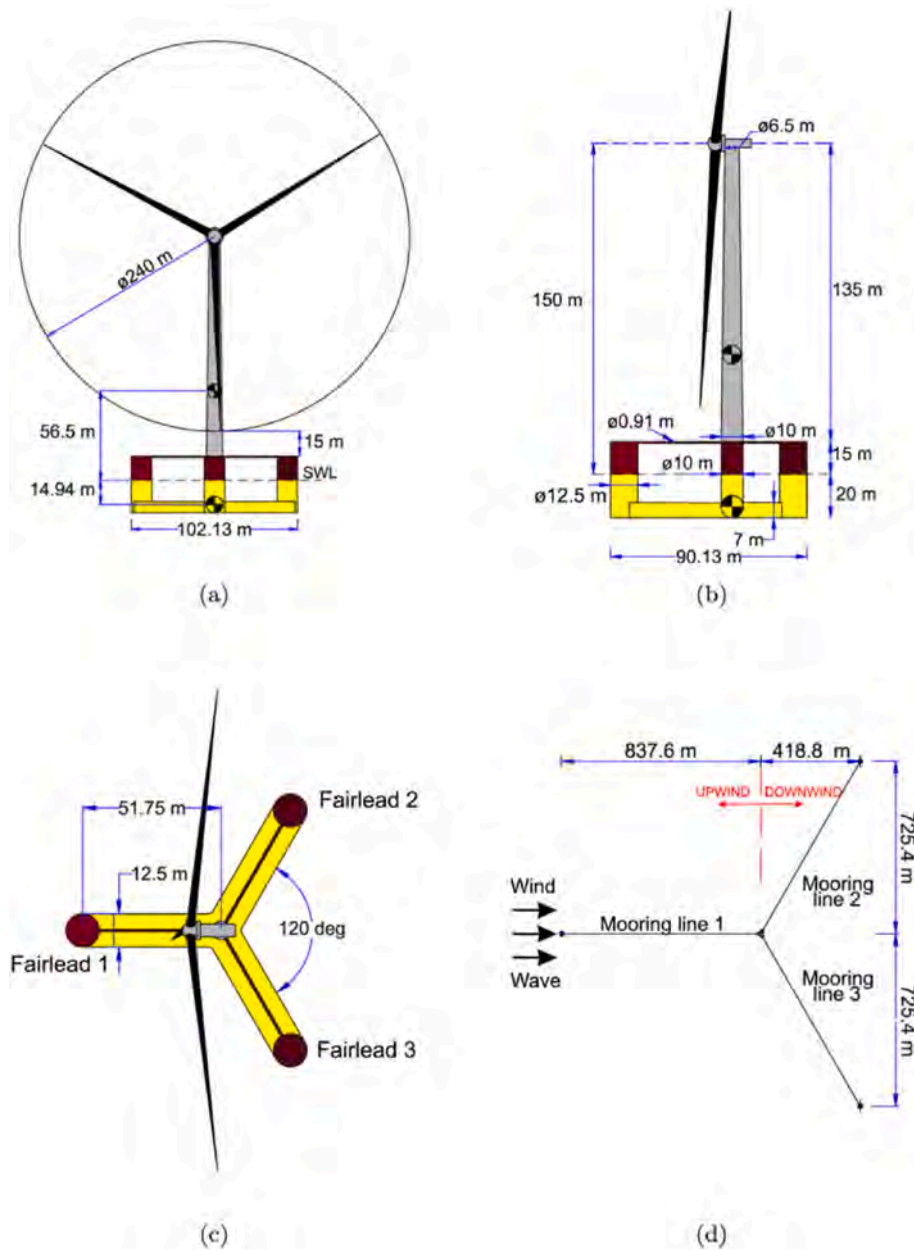
Fig. 21. Schematic of the IEA 15 MW wind turbine mounted on the VolturnUS-S semi-submersible platform: (a) Front view; (b) Side view; (c) Top view; (d) Plan view of the mooring system.

Table 8
Main parameters of the VolturnUS-S semi-submersible platform.

Parameter	Value
Depth of platform base below SWL	20 m
Elevation of central column above SWL	15 m
Displacement	20206.0 m^3
Mass (including ballast)	1.7854×10^7 kg
Center of mass location below SWL	14.94 m
Platform roll inertia about CM	1.251×10^{10} kg m^2
Platform pitch inertia about CM	1.251×10^{10} kg m^2
Platform yaw inertia about centerline	2.367×10^{10} kg m^2

Table 9
Main parameters of the mooring system for the VolturnUS-S semi-submersible platform.

Parameter	Value
Unstretched length	850.0 m
Volume-equivalent diameter	0.3330 m
Equivalent mass density	685.00 kg/m
Equivalent axial stiffness	3.270×10^9 N
Normal drag coefficient	1.11
Tangential drag coefficient	0.20
Normal Added mass coefficient	0.82
Tangential added mass coefficient	0.27

and 300 m in the x, y and z coordinates, respectively. The wave propagates from the leftmost boundary to the outlet at the rightmost, and the platform locates 300 m downstream of the wavemaker. A medium density mesh is generated as plotted in Fig. 23. More numerical details including the mesh convergence study are referred to Zhong et al.

(2023).

The LDG FEM, PEM, catenary and QS mooring line models are coupled to OpenFOAM to form the hydro-mooring models. In all the couplings, the mooring attachment points on the platform are used as
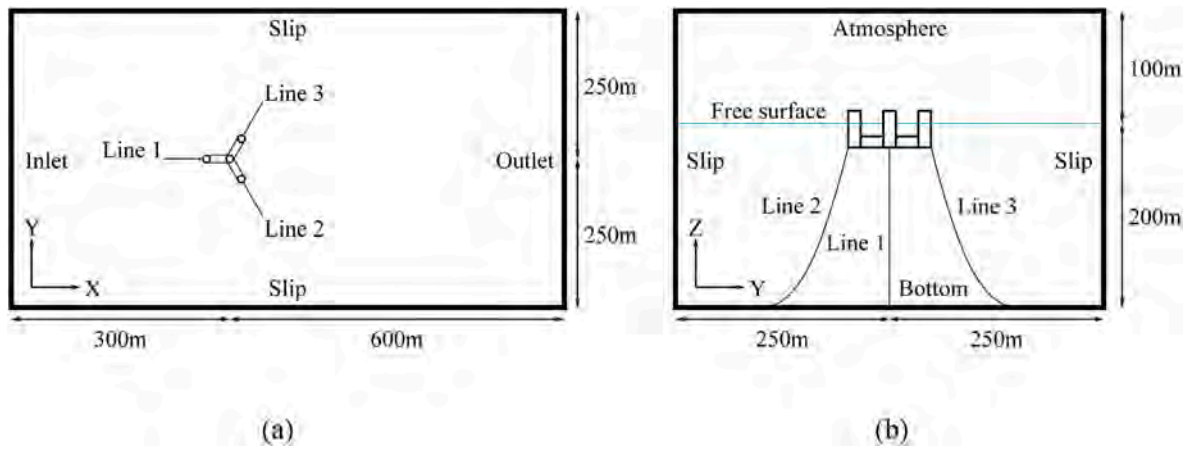
Fig. 22. Computational domain of the dynamic responses of the VolturnUS-S semi-submersible platform under waves: (a) View from top; (b) View from outlet.
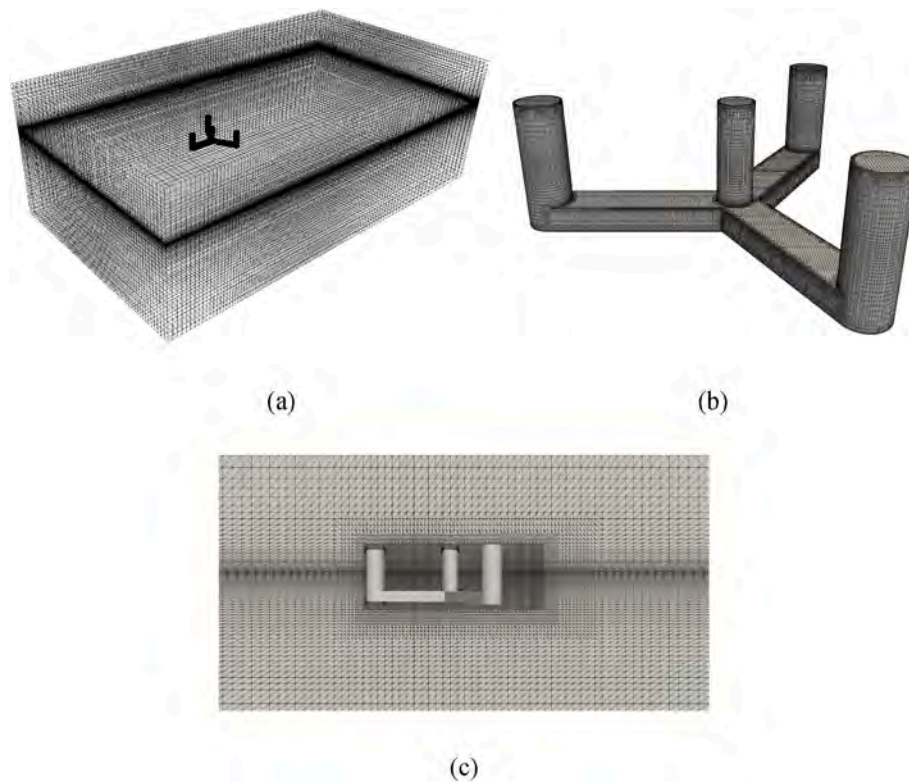

Fig. 23. Mesh arrangement for the dynamic responses of the VolturnUS-S semi-submersible platform under waves: (a) Global view; (b) Local view; (c) Cutaway view.

Dirichlet boundary conditions for the mooring solvers. And the resultant force from each mooring line is returned to the CFD solver for the rigid body dynamics. The CFD-FEM, CFD-PEM and CFD-catenary models are built with the rigidBodyDynamics class of OpenFOAM while the CFD-QS are built with the sixDoFRigidBodyMotion class due to the mooring code structures. The CFD-PEM and CFD-catenary models are implemented by the authors. Details on the CFD-FEM and CFD-QS models are referred to Palm et al. (2017) and Chen and Hall (2022), respectively. For all the coupled simulations, convergence tests on the number of mooring line discretization elements have been conducted. Converged results can be obtained with 20, 170, 170 and 50 line segments for CFD-FEM, CFD-PEM, CFD-Catenary and CFD-QS models, respectively.

Two wave conditions, i.e., irregular waves with random and focused component phases, are selected. The irregular wave with a significant height of 6 m and a peak period of 15s is used. Frequency range between 0.04 Hz and 0.20 Hz is discretized into 32 pieces for reproducing the JONSWAP spectrum. For the focused wave, the focusing time and location are 100s and 300 m, respectively. Details on the generation of focused waves are referred to Zhong et al. (2023).

5.3. Platform motion response

The motion responses in surge, heave and pitch of the semi-submersible platform under irregular and focused waves are shown in Figs. 24 and 25, respectively. The results obtained with the four hydro-mooring models are compared in the figures. It is seen that the platform undergoes irregular movements in the irregular wave case while the motion exhibits focusing behaviors as the wave in the focused wave case. In both cases, the CFD-PEM model gives the largest predictions particularly in surge and heave. In specific, the floating platform surges
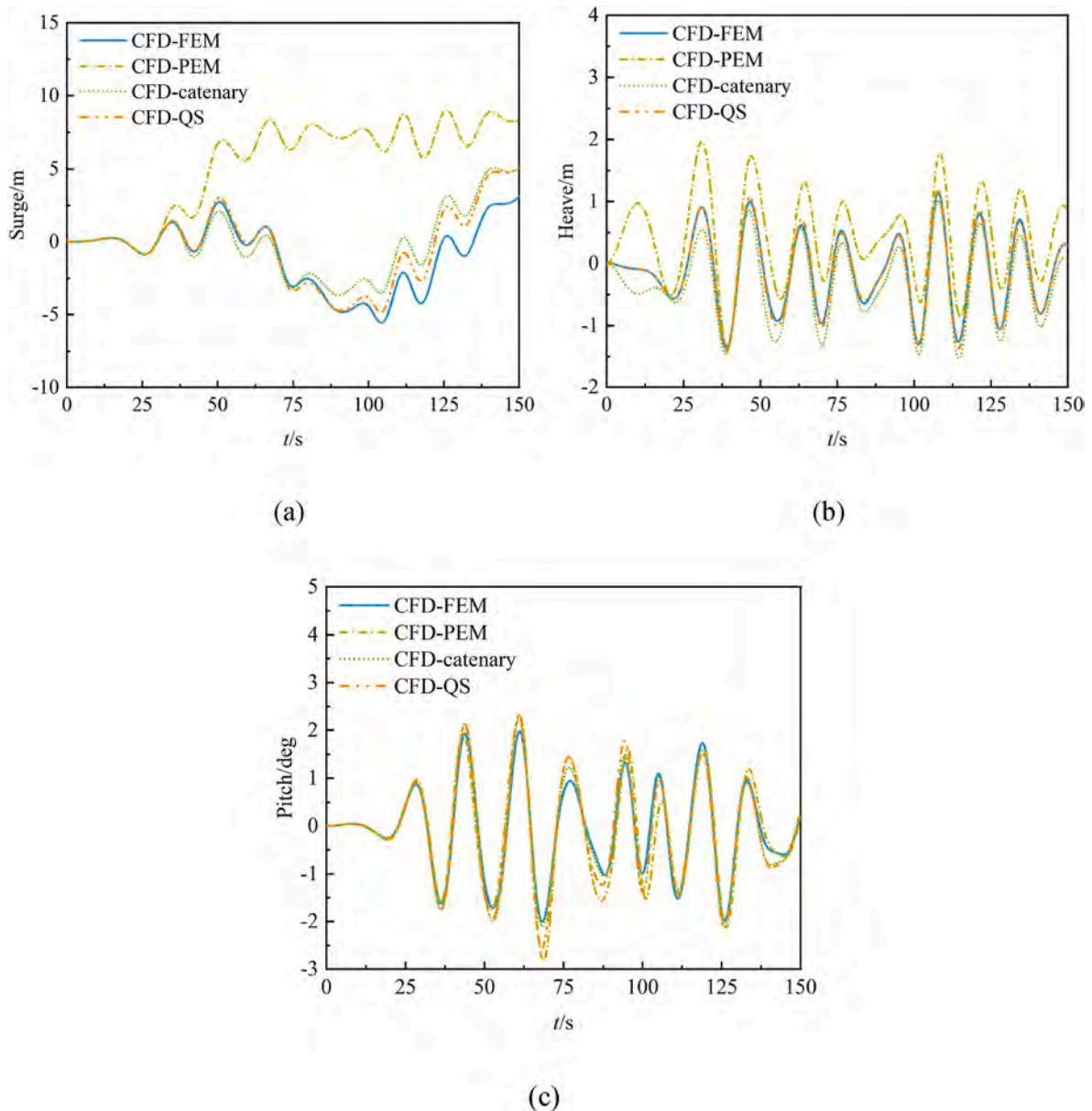
Fig. 24. Motion responses of the VolturnUS-S semi-submersible platform under the irregular wave: (a) Surge; (b) Heave; (c) Pitch.

to the farthest downstream when using PEM as the mooring model. And both the mean position and amplitude of the heave motion are increased to the most among the coupled models. These are related to the simulated mooring line profiles in PEM results and will be discussed in section 5.5. For the CFD-catenary model, the responses of the platform tend to be underpredicted. As seen in Figs. 24 and 25, the motion curves obtained with the CFD-catenary model are visibly lower than those obtained with the CFD-FEM model except for the surge in irregular wave condition. The results are thought to be related to the ignorance of axial stiffness in the catenary mooring model, which uses constant cable length to form the line shape throughout. The fact that longer line segments are to be lifted when stiff cable is used explains the higher mooring forces. The mooring line fairlead tension when the platform is at the initial position evaluated by the four hydro-mooring models are shown in Table 10. The table confirms that the catenary model gives the largest mooring line tension among the models. Besides, the mooring tension predicted by PEM is the lowest and is even less than half of that obtained by FEM. This is in accordance with the observations on the motion results in Figs. 24 and 25. The QS predicted tension shows the

best match to the FEM result in Table 10. In Figs. 24 and 25, the motion responses predicted by the CFD-QS model also exhibit the best agreement with those of the CFD-FEM model. But it is pointed out that the surge response given by the CFD-QS model is overestimated in the irregular wave case and underestimated in the focused wave case. In heave response, nearly identical results are shown between the CFD-QS and CFD-FEM models in both wave cases while in pitch response, the amplitudes of motion are enlarged with the CFD-QS model.

5.4. Mooring line fairlead tension

The time series of the mooring line fairlead tension under irregular and focused waves are shown in Figs. 26 and 27, respectively. Only the results of mooring lines 1 and 2 are plotted because of the symmetry of the configuration. It is seen that in both wave conditions, fairlead tensions of both mooring lines given by the CFD-catenary model are visibly higher than those of the CFD-FEM model, while the results obtained by the CFD-PEM model are significantly lower than all other coupled models. The CFD-QS model shows the best match to the CFD-FEM model
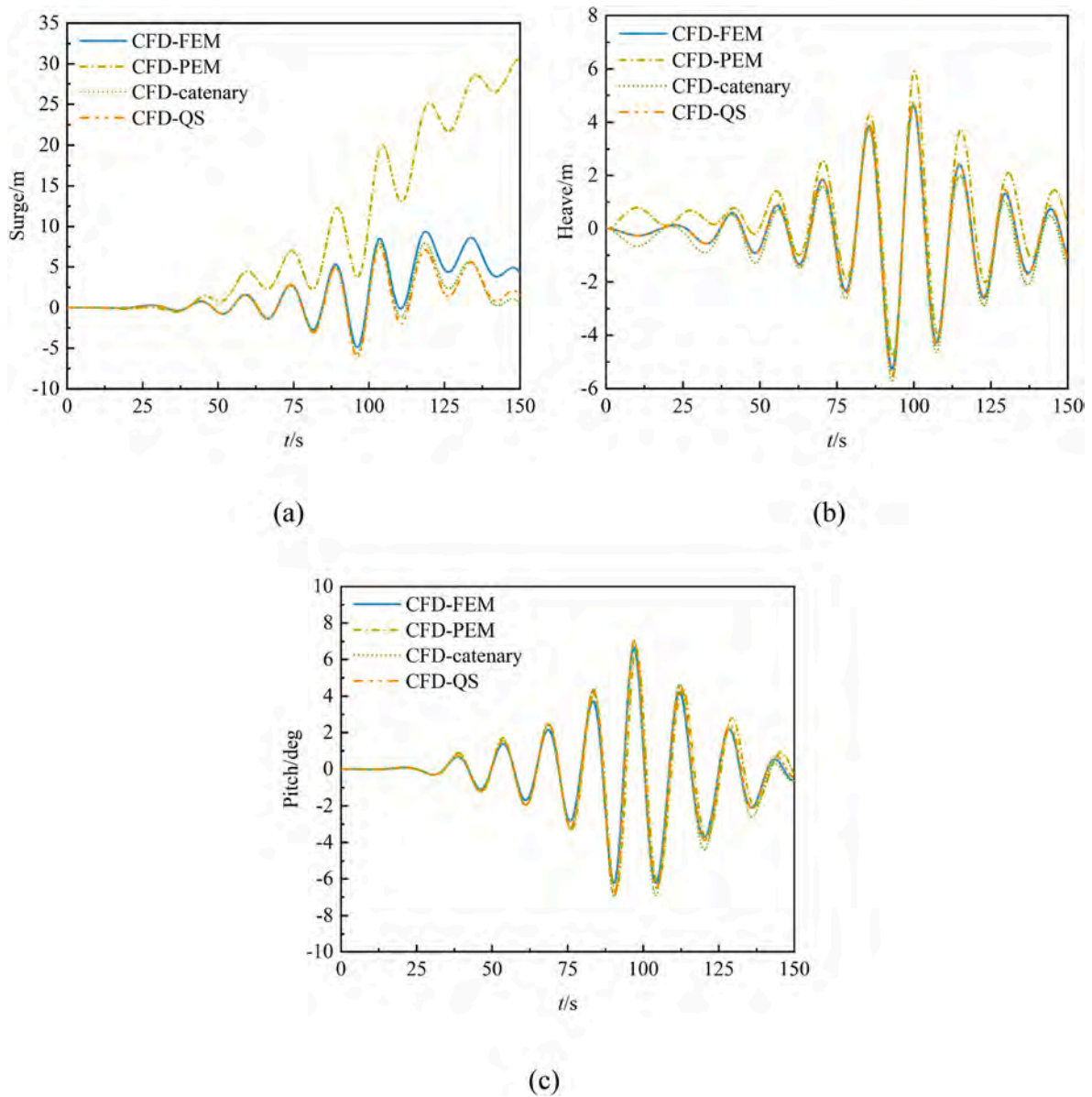
Fig. 25. Motion responses of the VolturnUS-S semi-submersible platform under the focused wave: (a) Surge; (b) Heave; (c) Pitch.

Table 10
The mooring line fairlead tension at the initial platform position.

Coupled models	Mooring line fairlead tension
CFD-FEM	2436.4 KN
CFD-PEM	1223.1 KN
CFD-catenary	2824.4 KN
CFD-QS	2443.8 KN

in mooring line tension predictions in Figs. 26 and 27 though the amplitudes of tension variations are visibly larger when the mooring dynamics is included.

Moreover, it is seen in Figs. 26 and 27 that the variations of the mooring line fairlead tensions predicted by the CFD-PEM, CFD-catenary and CFD-QS models are generally in phase with each other while the mooring tension time series given by the CFD-FEM show noticeably different phase property. This is apparently due to the nonlinearity in the mooring dynamics of the FEM model. To further analyze the relation between the mooring line fairlead tension and the platform motions, these two types of results obtained by the four models are plotted

together in Fig. 28. It is seen in Fig. 28 that for the three mooring line models which exclude dynamics, the mooring tension variations generally follow the motions in surge but with small phase lags. This is consistent with Niranjan and Ramisetti (2022) which states that the crests and troughs in mooring tensions are the same as the variations in platform surge. The facts that the motions in the three degrees of freedom (DOFs) in longitudinal plane can all contribute to the mooring system reactions and there are phase differences between the three types of motions shown in Fig. 28(b)–(d) explain the phase lags. An analysis on the phase differences between motions in focused wave condition is referred to the previous work of the authors (Zhong et al., 2023). For the dynamic mooring model, no clear correlation between the simulated mooring tension and platform surge is identified. As the mooring dynamics is additionally influenced by fluid added mass and drag, nonlinearity arises in the dynamic model. And this modifies the phases in the mooring forces.

5.4.1. Mooring line profile
As the mooring tension is related to the lifted mooring line above sea bottom, the mooring line profile is examined. The profiles of mooring
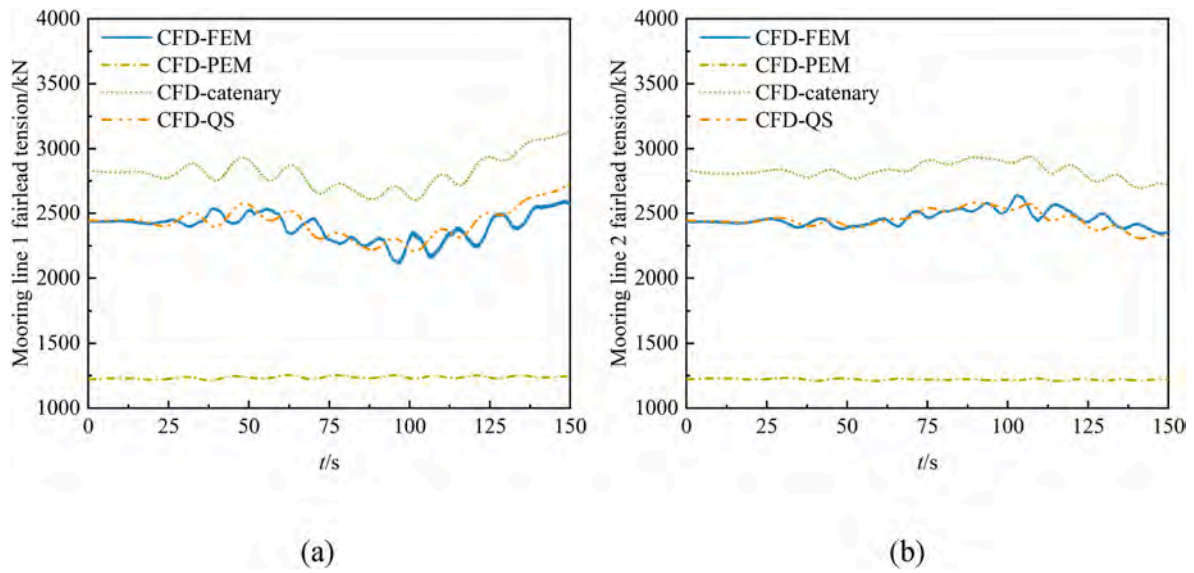
Fig. 26. Mooring line fairlead tension of the VolturnUS-S semi-submersible platform under the irregular wave: (a) Mooring line 1; (b) Mooring line 2.
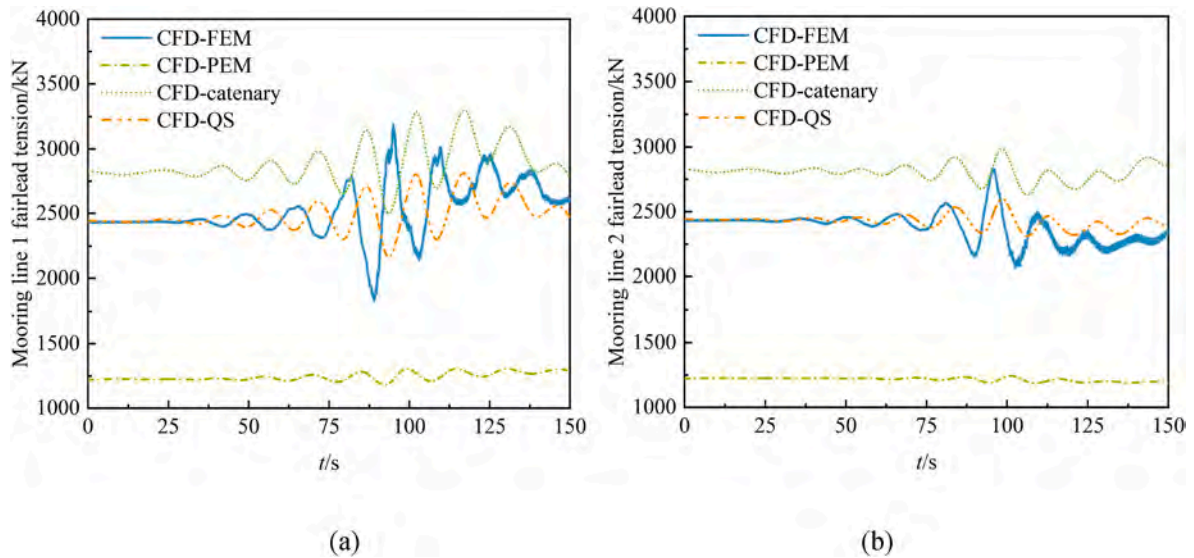

Fig. 27. Mooring line fairlead tension of the VolturnUS-S semi-submersible platform under the focused wave: (a) Mooring line 1; (b) Mooring line 2.

line 1 at the times 95s and 103s in the focused wave condition are shown in Fig. 29. The results obtained by the CFD-QS model are not shown since the node position output is not available. The selected two times correspond to the instants when the mooring line fairlead tension given by the CFD-FEM model obtains local maximum and minimum as shown in Fig. 27(a).

It is first seen in Fig. 29 that the lifted mooring line shows a completely different shape in the CFD-PEM model comparing to other models. The suspended line has the least length among the models and the reacting force is also the lowest as demonstrated in Fig. 27. The reason may lie in the PEM procedure, in which the extrapolation proceeds from the fairlead to the anchor and the loop repeats until the error in computed to real anchor positions is lower than a preset value. This scheme gives a line shape which tends to be vertically suspended other than catenary. The mooring line profiles simulated by the CFD-FEM and CFD-catenary models show general agreement in Fig. 29. But it is observed that there exists notable mismatch over the line range touching the sea bottom. This is in fact due to the overall mooring shape condition. The mooring dynamics considered in CFD-FEM contributes to the

nonlinearity in the mooring line motion which alters the phases of the line profile. The difference in status of the mooring line profile leads to the phase difference in mooring force shown in Fig. 27.

6. Conclusions

In this study, six mooring line models are compared with the aim of obtaining deep insights into performances of the models. The line models include three dynamics ones, i.e., the LDG FEM of Moody, the LM of MoorDyn and the FDM of OpenMOOR, and three QS ones, i.e., the PEM, the catenary and the QS of MAP. The Moody, MoorDyn, OpenMOOR and MAP are open-source or semi open-source codes while the PEM and catenary models are developed by the research group of the authors. Three groups of tests including catenary cable subjected to fairlead excitation, hanging cable under axial excitation and FOWT in waves are carried out. The first two test groups focus on single line dynamics to analyze among the three dynamic models while the third test group focuses on coupled hydro-mooring modeling with the FEM, PEM, catenary and QS coupled to OpenFOAM. The test results show that
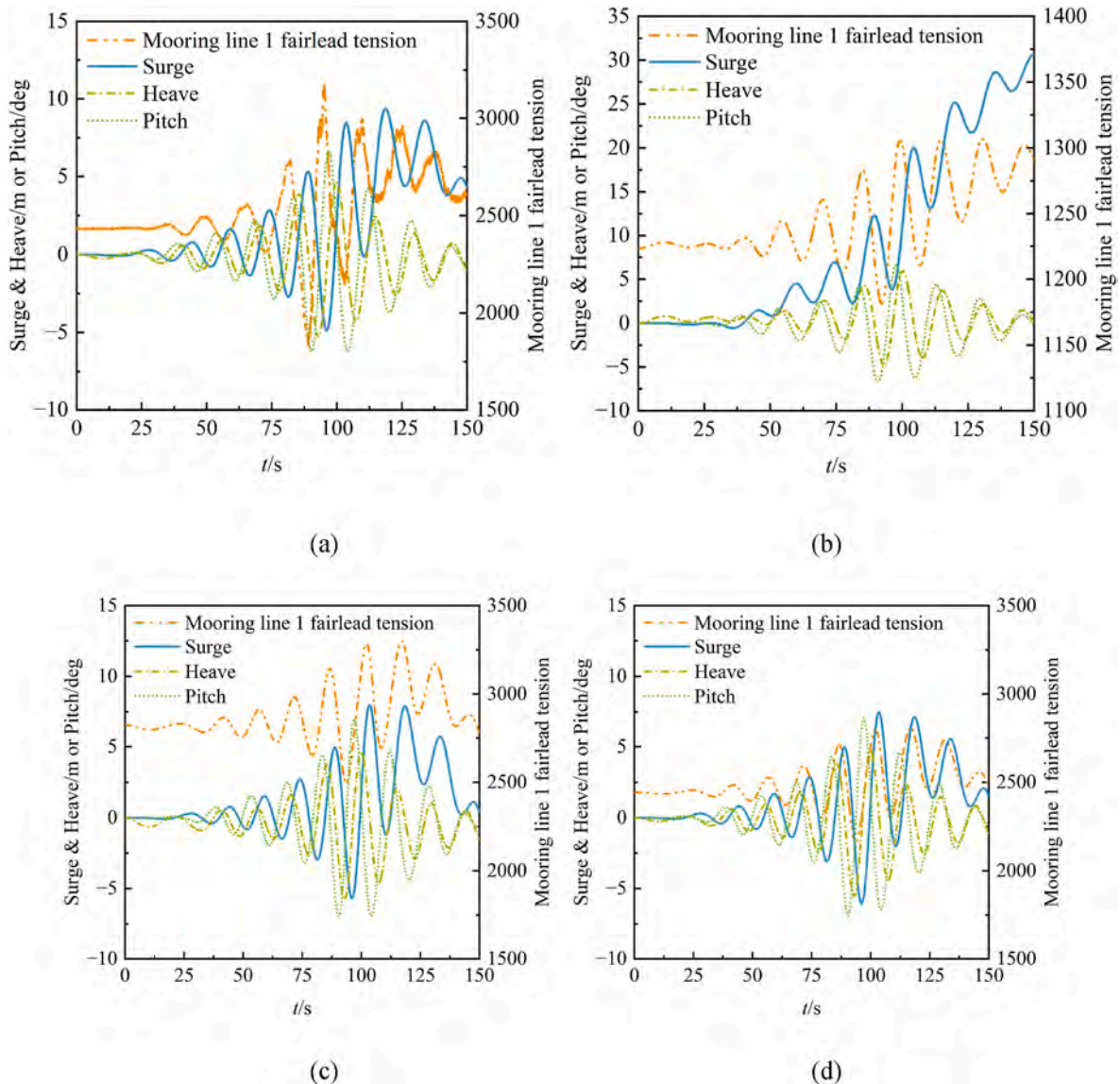
Fig. 28. Comparison of variation phase between the mooring line fairlead tension and the platform motions for the VolturnUS-S semi-submersible platform under the focused wave: (a) The CFD-FEM model; (b) The CFD-PEM model; (c) The CFD-catenary model; (d) The CFD-QS model.

there are substantial differences among the models in various scenarios. The main conclusions are summarized in the following.

1. For the dynamics of a single catenary cable under fairlead excitation, the three dynamic mooring line models, i.e., LDG FEM, LM and FDM, all give satisfactory predictions for low and intermediate frequency mooring dynamics. But for high frequency mooring dynamics, the accuracies of LM and FDM reduce especially for the snap loading condition. Overall, the LDG FEM exhibits the best performance among the three dynamic models. However, one deficiency of LDG FEM is the unpredictable slight tension fluctuations over the motion cycle, the cause of which need further investigations. Moreover, the most efficient model is the LDG FEM since modal basis other than nodal basis is used in the FEM formulation, and the least efficient is the FDM whose time cost is several times of those of LDG FEM and LM. For coupling the mooring dynamics model to a floating structure numerical model in realistic applications, the LDG FEM and LM are recommended.

2. For the dynamics of a single hanging cable with axial excitation, when the lower end is free with a spherical payload, both LDG FEM and LM underestimate the fluctuation amplitude in the low frequency case. In the high frequency case when snap loads occur, the results of LDG FEM and LM are closely related to the tangential drag and internal damping, respectively. For the similar hanging cable test but with the lower end fixed, the LDG FEM and LM give identical results. Results reveal that Neumann boundary conditions weaken the robustness of LDG FEM and LM. Moreover, FDM fails for the axial loading scenarios due to the capability of the model and a high requirement on the mooring line to be catenary.

3. For the hydrodynamics of the IEA 15 MW semi-submersible FOWT under irregular and focused waves, four hydro-mooring models are established with the FEM, PEM, catenary and QS coupled to Open-FOAM. In both wave conditions, the CFD-PEM model gives the largest predictions which are related to the simulated mooring line profiles in PEM results. The CFD-catenary model tends to under-predict the dynamic responses which is thought to be related to the ignorance of axial stiffness in the catenary mooring model. The CFD-QS predictions show the best match to the CFD-FEM results but with smaller variation amplitude in mooring line fairlead tension. More-over, the CFD-PEM, CFD-catenary and CFD-QS models which exclude dynamics predict generally in phase mooring tensions which follow the platform surge motions. The inclusion of mooring
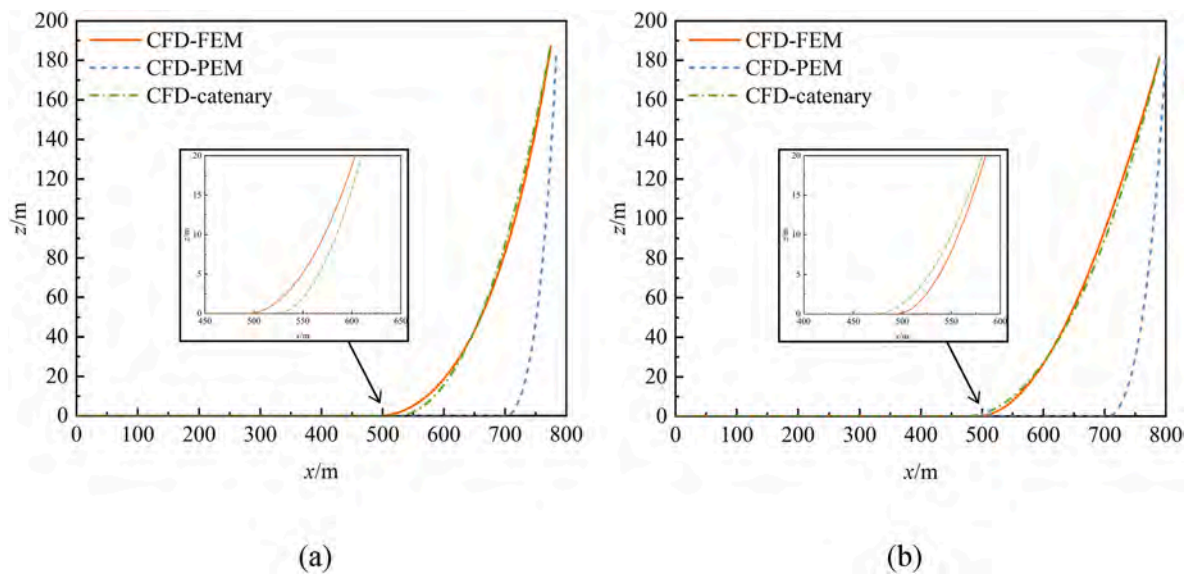
Fig. 29. The instantaneous profiles of mooring line 1 of the VolturnUS-S semi-submersible platform under the focused wave: (a) $t = 95s$; (b) $t = 103s$.

dynamics in CFD-FEM modifies the phases in mooring forces and introduces nonlinearity to the dynamics.

Funding

CRediT authorship contribution statement

Wenjie Zhong: Data curation, Formal analysis, Investigation, Methodology, Software. **Weiwen Zhao:** Data curation, Formal analysis, Investigation, Project administration, Software, Validation, Visualization, Writing – review & editing. **Decheng Wan:** Conceptualization, Funding acquisition, Project administration, Resources, Software, Supervision, Writing – review & editing. **Yan Zhao:** Data curation, Validation, Visualization.

Declaration of competing interest

The authors declare that they have no known competing financial interests or personal relationships that could have appeared to influence the work reported in this paper.

Data availability

Data will be made available on request.

Acknowledgement

References

Aamo, O.M., Fossen, T.I., 2000. Finite element modelling of mooring lines. Math. Comput. Simulat. 53 (4–6), 415–422.

Allen, C., Viscelli, A., Dagher, H., Goupee, A., Gaertner, E., Abbas, N., Hall, M., Barter, G., 2020. Definition of the UMaine VolturnUS-S Reference Platform Developed for the IEA Wind 15-megawatt Offshore Reference Wind Turbine (No.). National Renewable Energy Lab. (NREL), Golden, CO (United States). University of Maine, Orono, ME (United States), NREL/TP-5000-76773.

Antonutti, R., Peyrard, C., Johanning, L., Incecik, A., Ingram, D., 2016. The effects of wind-induced inclination on the dynamics of semi-submersible floating wind turbines in the time domain. Renew. Energy 88, 83–94.

Azcona, J., Munduate, X., González, L., Nygaard, T.A., 2017. Experimental validation of a dynamic mooring lines code with tension and motion measurements of a submerged chain. Ocean. Eng. 129, 415–427.

Barter, G.E., Darmofal, D.L., 2010. Shock capturing with PDE-based artificial viscosity for DGFEM: Part I. Formulation. J. Comput. Phys. 229 (5), 1810–1827.

Bernard, P.E., 2008. Discontinuous Galerkin Methods for Geophysical Flow Modeling, PhD Thesis. Universite catholique de Louvain.

Buckham, B., Driscoll, F.R., Nahon, M., 2004. Development of a finite element cable model for use in low-tension dynamics simulation. J. Appl. Mech. 71 (4), 476–485.

Chen, L., Basu, B., Nielsen, S.R., 2018. A coupled finite difference mooring dynamics model for floating offshore wind turbine analysis. Ocean. Eng. 162, 304–315.

Chen, H., Hall, M., 2022. CFD simulation of floating body motion with mooring dynamics: coupling MoorDyn with OpenFOAM. Appl. Ocean Res. 124, 103210.

Cheng, P., Huang, Y., Wan, D., 2019. A numerical model for fully coupled aero-hydrodynamic analysis of floating offshore wind turbine. Ocean. Eng. 173, 183–196.

Cockburn, B., Shu, C.W., 2001. Runge-Kutta discontinuous Galerkin methods for convection-dominated problems. J. Sci. Comput. 16, 173–261.

Dai, J., Hu, W., Yang, X., Yang, S., 2018. Modeling and investigation of load and motion characteristics of offshore floating wind turbines. Ocean. Eng. 159, 187–200.

Escalante, M.R., Sampaio, R.R., Rosales, M.B., Ritto, T., 2011. A reduced order model of a 3D cable using proper orthogonal decomposition. Mecanica Computacional 30 (13), 1143–1158.

Gaertner, E., Rinker, J., Sethuraman, L., Zahle, F., Anderson, B., Barter, G., Abbas, N., Meng, F., Bortolotti, P., Skrzypinski, W., Scott, G., Feil, R., Bredmose, H., Dykes, K., Shields, M., Allen, C., Viselli, A., 2020. IEA Wind TCP Task 37: Definition of the IEA 15-Megawatt Offshore Reference Wind Turbine. National Renewable Energy Lab. (NREL), Golden, CO (United States). NREL/TP-5000-75698.

Gobat, J.I., Grosenbaugh, M.A., 2001. Application of the generalized-a method to the time integration of the cable dynamics equations. Comput. Methods Appl. Mech. Eng. 190 (37–38), 4817–4829.

Gobat, J.I., Grosenbaugh, M.A., 2006. Time-domain numerical simulation of ocean cable structures. Ocean. Eng. 33 (10), 1373–1400.

Hall, M., Buckham, B., Crawford, C., 2014. Evaluating the importance of mooring line model fidelity in floating offshore wind turbine simulations. Wind Energy 17 (12), 1835–1853.

Hall, M., Goupee, A., 2015. Validation of a lumped-mass mooring line model with DeepCwind semisubmersible model test data. Ocean. Eng. 104, 590–603.

Hermawan, Y.A., Furukawa, Y., 2020. Coupled three-dimensional dynamics model of multi-component mooring line for motion analysis of floating offshore structure. Ocean. Eng. 200, 106928.

Huang, S., 1994. Dynamic analysis of three-dimensional marine cables. Ocean. Eng. 21 (6), 587–605.

Huang, Y., Zhuang, Y., Wan, D., 2021. Hydrodynamic study and performance analysis of the OC4-DeepCwind platform by CFD method. Int. J. Comput. Methods 18 (4), 2050020.

Jiang, C., el Moctar, O., Paredes, G.M., Schellin, T.E., 2020. Validation of a dynamic mooring model coupled with a RANS solver. Mar. Struct. 72, 102783.

Jonkman, J.M., 2009. Dynamics of offshore floating wind turbines-model development and verification. Wind Energy: An International Journal for Progress and Applications in Wind Power Conversion Technology 12 (5), 459–492.

Kallesøe, B.S., Hansen, A.M., 2011. Dynamic mooring line modeling in hydro-aero-elastic wind turbine simulations. In: International Ocean and Polar Engineering Conference. ISOPE-I.

Khan, N.U., Ansari, K.A., 1986. On the dynamics of a multicomponent mooring line. Comput. Struct. 22 (3), 311–334.

Krivodonova, L., Xin, J., Remacle, J.F., Chevaugeon, N., Flaherty, J.E., 2004. Shock detection and limiting with discontinuous Galerkin methods for hyperbolic conservation laws. Appl. Numer. Math. 48 (3–4), 323–338.

Li, C.B., Choung, J., 2021. Effects of strain-and strain rate-dependent nonlinear mooring line stiffness on floating platform motion. Ocean. Eng. 241, 110011.

Li, X., Guo, X., Guo, H., 2018. Vector form intrinsic finite element method for nonlinear analysis of three-dimensional marine risers. Ocean. Eng. 161, 257–267.

Liu, Y., Xiao, Q., Incecik, A., Peyrard, C., Wan, D., 2017. Establishing a fully coupled CFD analysis tool for floating offshore wind turbines. Renew. Energy 112, 280–301.

Liu, Y., Xiao, Q., Incecik, A., Peyrard, C., 2019. Aeroelastic analysis of a floating offshore wind turbine in platform-induced surge motion using a fully coupled CFD-MBD method. Wind Energy 22 (1), 1–20.

Masciola, M., Jonkman, J., Robertson, A., 2013a. Implementation of a multisegmented, quasi-static cable model. In: International Ocean and Polar Engineering Conference. ISOPE-I.

Masciola, M., Robertson, A., Jonkman, J., Coulling, A., Goupee, A., 2013b. Assessment of the importance of mooring dynamics on the global response of the DeepCwind floating semisubmersible offshore wind turbine. In: International Ocean and Polar Engineering Conference. ISOPE-I.

Matha, D., Fechter, U., Kuhn, M., Cheng, P.W., 2011. Non-linear Multi-Body Mooring System Model for Floating Offshore Wind Turbines. EWEA offshore.

Montano, A., Restelli, M., Sacco, R., 2007. Numerical simulation of tethered buoy dynamics using mixed finite elements. Comput. Methods Appl. Mech. Eng. 196 (41–44), 4117–4129.

Nakajima, T., Motora, S., Fujino, M., 1982. On the dynamic analysis of multi-component mooring lines. In: Offshore Technology Conference, pp. OTC–4309.

Niranjan, R., Ramisetti, S.B., 2022. Insights from detailed numerical investigation of 15 MW offshore semi-submersible wind turbine using aero-hydro-servo-elastic code. Ocean. Eng. 251, 111024.

Palm, J., Eskilsson, C., Bergdahl, L., 2017. An hp-adaptive discontinuous Galerkin method for modelling snap loads in mooring cables. Ocean. Eng. 144, 266–276.

Ren, Y., Venugopal, V., Shi, W., 2022. Dynamic analysis of a multi-column TLP floating offshore wind turbine with tendon failure scenarios. Ocean. Eng. 245, 110472.

Robertson, A., Jonkman, J., Masciola, M., Song, H., Goupee, A., Coulling, A., Luan, C., 2014a. Definition of the Semisubmersible Floating System for Phase II of OC4. National Renewable Energy Lab. (NREL), Golden, CO (United States). NREL/TP-5000-60601.

Robertson, A., Jonkman, J., Vorpahl, F., Popko, W., Qvist, J., Froyd, L., Chen, X., Azcona, J., Uzunoglu, E., Guedes Soares, C., Luan, C., 2014b. Offshore code comparison collaboration continuation within IEA wind task 30: phase II results regarding a floating semisubmersible wind system. In: International Conference on Offshore Mechanics and Arctic Engineering, vol. 45547. American Society of Mechanical Engineers. V09BT09A012.

Rodriguez Luis, A., Armesto, J.A., Guanche, R., Barrera, C., Vidal, C., 2020. Simulation of marine towing cable dynamics using a finite elements method. J. Mar. Sci. Eng. 8 (2), 140.

Suhara, T., Koterayama, W., Tasai, F., Hiyama, H., Sao, K., Watanabe, K., 1981. Dynamic behavior and tension of oscillating mooring chain. In: Offshore Technology Conference. OnePetro.

Touzon, I., Nava, V., Gao, Z., Mendikoa, I., Petuya, V., 2020. Small scale experimental validation of a numerical model of the HarshLab2.0 floating platform coupled with a non-linear lumped mass catenary mooring system. Ocean. Eng. 200, 107036.

Tran, T.T., Kim, D.H., 2015. The coupled dynamic response computation for a semi-submersible platform of floating offshore wind turbine. J. Wind Eng. Ind. Aerod. 147, 104–119.

Tran, T.T., Kim, D.H., 2016. Fully coupled aero-hydrodynamic analysis of a semi-submersible FOWT using a dynamic fluid body interaction approach. Renew. Energy 92, 244–261.

Walton, T.S., Polachek, H., 1959. Calculation of Nonlinear Transient Motion of Cables, vol. 65. Department of the Navy, David Taylor Model Basin.

Wilhelmy, V., Fjeld, S., Schneider, S., 1981. Non-linear response analysis of anchorage systems for compliant deep water platforms. In: Offshore Technology Conference. OTC-4051.

Wu, H., Zeng, X., Xiao, J., Yu, Y., Dai, X., Yu, J., 2020. Vector form intrinsic finite-element analysis of static and dynamic behavior of deep-sea flexible pipe. Int. J. Nav. Archit. Ocean Eng. 12, 376–386.

Zhang, Y., Shi, W., Li, D., Li, X., Duan, Y., 2022a. Development of a numerical mooring line model for a floating wind turbine based on the vector form intrinsic finite element method. Ocean. Eng. 253, 111354.

Zhang, Y., Shi, W., Li, D., Li, X., Duan, Y., Verma, A.S., 2022b. A novel framework for modeling floating offshore wind turbines based on the vector form intrinsic finite element (VFIFE) method. Ocean. Eng. 262, 112221.

Zhong, W., Zhang, X., Wan, D., 2023. Hydrodynamic characteristics of a 15 MW semi-submersible floating offshore wind turbine in freak waves. Ocean. Eng. 283, 115094.

Zhu, Z.H., 2010. Dynamic modeling of cable system using a new nodal position finite element method. International journal for numerical methods in biomedical engineering 26 (6), 692–704.